Characteristics of Silicon Photomultiplier at cryogenic temperatures

Master's thesis
University of Turku
Department of Physics
and Astronomy
Physics
2024
Tom Kiilerich
Supervisor:
dos. Sergey Vasiliev

UNIVERSITY OF TURKU
Department of Physics and Astronomy

KIILERICH, TOM: Characteristics of Silicon Photomultiplier at cryogenic temperatures

Master's thesis, 51 p.
Physics
2024

We are conducting optical 1S-2S spectroscopy of magnetically trapped atomic hydrogen at ultra-low temperatures. For this an optical diagnostic scheme which is operational in a dilution refrigerator at temperatures below 1 K is required.

In this thesis we discuss the theory behind Silicon Photomultipliers (SiPMs) and how their properties are affected at cryogenic temperatures. We describe the operation and characterization of SiPMs at various cryogenic temperatures, down to 180 mK. We show the temperature dependence of the signal shape, breakdown voltage, microcell capacitance and gain, dark count rate and photon detection efficiency, concluding that SiPMs can be effectively used at ultra-low temperatures with sensitivity at the single photon level.

Below 40 K we observed a secondary breakdown in the SiPM due to a quantum tunneling effect, which set an upper limit for the bias voltage operating region. Assessment of the damage to the SiPM due to thermal cycles shows that the SiPM can withstand multiple cooling cycles without losing its efficiency.

Keywords: Silicon Photomultiplier, SiPM, light detection, single photon detection, optical spectroscopy, cryogenic temperatures

Contents

Introduction

This thesis is written as a part of the research conducted by the Atomic Hydrogen Group of the Wihuri Physical Laboratory, the main topic of which is an experimental study of atomic hydrogen. One of the goals is the optical 1S-2S spectroscopy of magnetically trapped atomic hydrogen at ultra-low temperatures. The optical diagnostics requires sensitive detectors of light operating at cryogenic temperatures and capable of detection efficiency at the single photon level.

The first direct detection of a single photon was done already in 1934 by a Radio Corporation of America group with a photomultiplier tube (PMT) [1]. PMTs are vacuum tubes containing a photocathode and an array of electrodes that amplify the current created by the incoming initial photons and produce a macroscopic measurable current as a result. While PMTs are still used today, they have been widely replaced with solid state photon detectors utilizing well studied materials such as silicon.

The silicon p-n junction transistor was developed in 1948 by Shockley and soon led to the first application of silicon photodiode by Russel Ohl [2]. The photocurrent amplification effect and avalanche breakdown of silicon was studied in 1950's [3, 4] and more sophisticated designs for solid state photodetectors started to emerge. The development of the first avalanche photodiode (APD) is credited to Jun-ichi Nishizawa in 1952 [5]. The theoretical and experimental work continued through the 1960's and the first device equivalent to a modern day Silicon Photomultiplier (SiPM) was fabricated by Haitz [6].

A Silicon Photomultiplier is essentially a two dimensional array of Single Photon Avalanche Detectors (SPAD) connected in parallel. A SiPM can have a density of up to 10 000 SPADs per square millimetre, each SPAD being operated in Geiger mode and capable of detecting a single photon. SPADs ability to count millions of photons per second combined with their high density makes SiPMs extremely compact photon detectors with high sensitivity and dynamic range. In addition SiPMs are immune to external magnetic fields, which are often present in different experiments, as is the case with optical spectroscopy of magnetically trapped atomic hydrogen.

SiPMs are widely studied and used in the room temperature range with an extensive amount of data available from their manufacturers. However, at cryogenic temperatures there is both a lack of theory as well as experimental results to fully characterize the properties of SiPMs. The basic properties of silicon, such as the structure of energy bands and charge carrier mobility, strongly depend on temperature and cause changes in the functionality of SiPMs [7]. Numerous applications in nuclear and particle physics as well as atomic spectroscopy require cryogenic temperatures setting new demands for photon detection. The objectives of the research, experimental setup and temperature range impose different demands for the photodetectors and thus testing and finding an optimal detector for each measurement scheme is a mandatory step.

This thesis aims to find a SiPM capable of operating in sub kelvin temperatures to be used in further quantum experiments with ultra-cold atomic hydrogen. While there exist earlier reports of SiPMs operated at temperatures down to 1 K, their properties below 1 K have not been investigated. A chip from Onsemi, MicroFJ-30035-TSV, was chosen as a candidate based on earlier positive results when the SiPM was operated at 4 K [8].

In the first chapter the photon detection mechanism in silicon is discussed and how it can be implemented in SPADs and SiPMs. Atomic properties of silicon are strongly dependent on the temperature and thus affect how SiPMs operate at cryogenic temperatures. These thermal effects will be reviewed in chapter one. Second chapter will go through the experimental methods and devices used in the experimental part of this thesis, and in the third chapter the experimental results obtained will be presented and compared to earlier reports.

1 Theory

To understand the working principle of a silicon photomultiplier, the atomic properties of silicon need to be reviewed first. Silicon is an elemental semiconductor and is widely used in all electronics. It has been studied extensively and detailed descriptions of its properties exists as well as comprehensive experimental data. The following chapter presents some basic semiconductor physics required to understand how SiPMs operate based on a textbook "Semiconductor Devices: Physics and Technology" by S.M. Sze and M.K. Lee [9], followed by a description of SPADs and SiPMs, their working principles and main parameters. In the end of the chapter the effects of cryogenic temperatures on these parameters is briefly discussed.

1.1 Energy band structure and doping of silicon atoms

Silicon has four valence electrons, two on the 3S orbital and two on the 3P orbital. When two silicon atoms get close to each other the orbitals can interact and form new orbitals in a process called hybridization. The silicon goes through SP3 hybridization and forms covalent bonds with four neighbouring atoms in a diamond lattice structure as shown in figure 1. The SP3 hybridization adds new energy levels for the silicon and when the number of silicon atoms in the crystal structure increases the energy levels will merge into two continuous energy bands called the valence and conduction band. At low temperatures the electrons are bound to the lattice structure and the electrons are located in the valence band. In these conditions silicon is effectively an insulator, since no electrons are available for conduction.

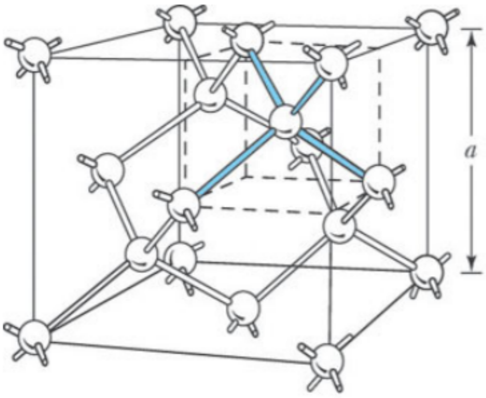

Figure 1: Diamond lattice of silicon atoms [9].

At higher temperatures the thermal vibrations of the lattice may be sufficiently high to break the covalent bond and excite an electron to the conduction band. When an electron is exited to the conduction band it leaves behind a hole in the valence band, creating an electron-hole pair. The hole can be filled by neighbouring electrons in the valence band, making the hole a positive charge carrier. Thus an excitation of an electron always creates two charge carriers. Creation of an electron-hole pair in silicon lattice is illustrated in figure 2.

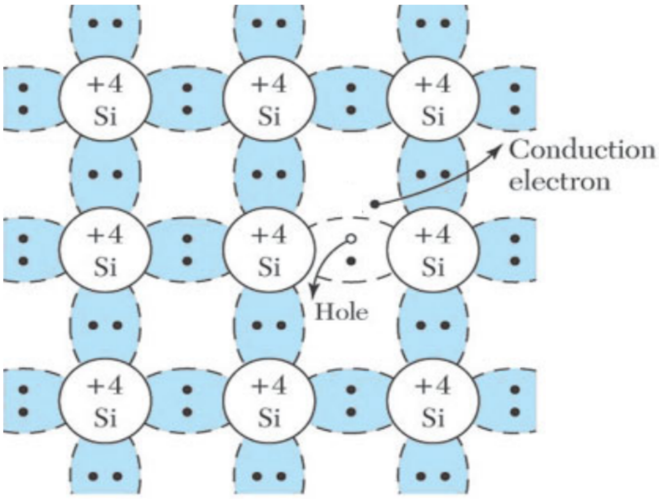

Figure 2: Electron-hole pair in silicon [9].

The energy required to create an electron-hole pair depends on the energy band structure of the silicon. The bottom edge of conduction band and the top edge of valence band are separated by the energy band gap E_g. Figure 3 shows a simplified energy band structure of silicon with an energy band gap of 1.12 eV, equivalent to a temperature of 13 000 K.

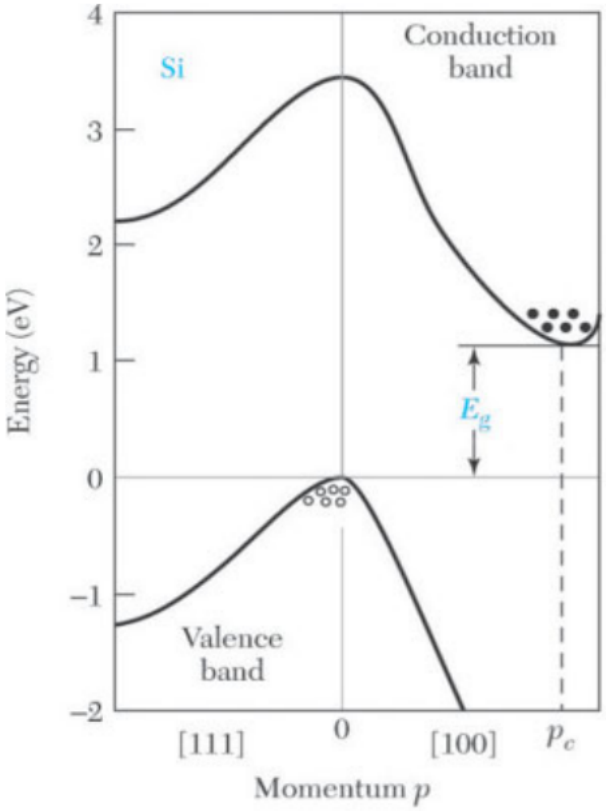

Figure 3: The band gap E_g is the separation of the bottom edge of the conduction band and the top edge of the valence band [9].

The probability for an electron to occupy an energy level E is determined by the Fermi-Dirac distribution

$$F(E) = \frac{1}{e^{(E-E_F)/kT} + 1}, \tag{1}$$

where k is the Boltzmann constant, T temperature and E_F the Fermi energy. For intrinsic semiconductors the Fermi level is located nearly midway between the conduction and valence bands. From equation (1) it can then be seen that in room temperature ($kT = 0.026$ eV) the probability for an electron to occupy the conduction band is low and silicon is a perfect insulator. The Fermi level can be increased or decreased by doping impurities to the crystal structure. These impurities will introduce new energy levels to the band structure and shift the Fermi level accordingly.

Silicon can be doped with either p-type (positive) or n-type (negative) doping. Replacing a silicon atom in the crystal structure with an acceptor (p-type) or a donor (n-type) changes the covalent bonds and creates an excess of either electrons or holes as shown in figure 4.

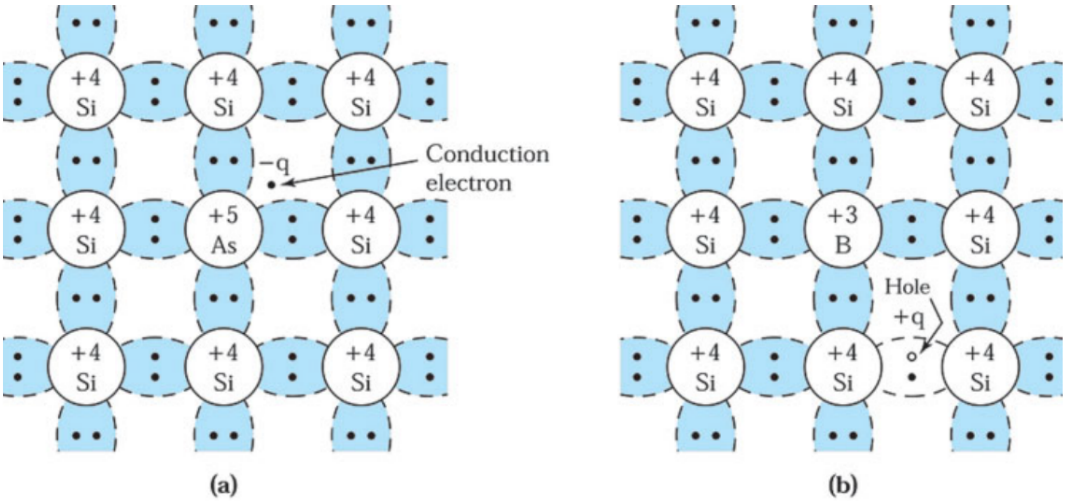

Figure 4: Schematic picture of silicon doped with a) n-type donor (arsenic) and b) p-type acceptor (boron) [9].

For a p-type doping a silicon atom is replaced with an atom having only three valence electrons (elements of group III: B, Ga, In), extra states with energies slightly above the top of the valence band are created. This moves the Fermi level closer to the valence band and allows the silicon atoms to be ionized with many orders of magnitude smaller energies (typical acceptor ionization energy is below 0.04 eV), thus creating holes to the valence band. The holes are majority charge carriers in p-type doping and carry positive charge in the semiconductor. N-type doping is similar but the impurities are atoms with five valence electrons (elements of group V: P, As, Sb). The fifth electron is weakly bound to the donor nucleus and its energy is very close to the bottom of the conduction band. The effective ionization energy is very low (below 0.03 eV), and the fifth electron is excited to the conduction band even at room temperature, leading to excessive and mobile negative charge.

P-types and n-types are extrinsic semiconductors since the majority charge carriers are due to the impurities. They remain electrically neutral but have greatly increased conductive properties. By changing the doping concentration the charge carrier density can be controlled. The individual extrinsic semiconductors are not that interesting, but by combining p-type and n-type semiconductors into a single crystal a p-n junction can be created. Next chapter will discuss the properties of a p-n junction and how it can be implemented as a photon detector.

1.2 Avalanche breakdown in silicon p-n junction

When fusing p-type and n-type semiconductors together they merge to produce a p-n junction. When first connected, there exists a large density gradient across the contact surface between the two different semiconductor types. As a result of diffusion the charge carriers will begin to migrate across the junction. The free electrons from the n-type silicon will drift to the p-type silicon and fill the holes in the valence band. Vice versa the holes from the p-type will drift to the n-type silicon and combine with the electrons. As a result the p-type will be left with negatively charged acceptor ions and the n-type with positively charged donor ions. This process continuously builds up electrical charge over the junction until the electric field is strong enough to repel further charge carriers from crossing over the junction and an equilibrium is reached. In equilibrium a depletion layer is created around the p-n

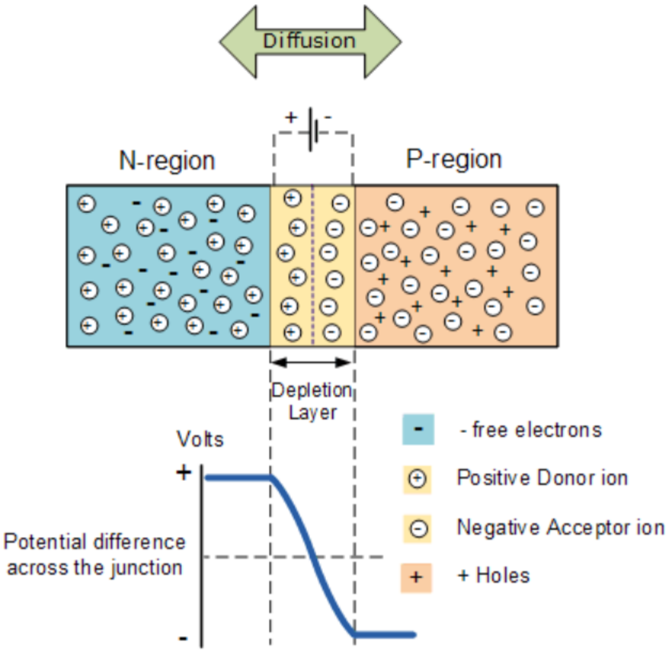

Figure 5: A schematic photo of a p-n junction in equilibrium. A depletion layer is formed around the junction with a steady potential gradient over it [10].

junction which is free of mobile charge carriers. Figure 5 illustrates the equilibrium in which the depletion layer is formed and the electric field over the junction is strong enough to prevent further diffusion. The n-region is positively charged with free electrons available as charge carriers and the p-region in contrast is negatively charged with holes available as charge carriers. The depletion layer is free of any mobile charge carriers.

The p-n junction can be operated in forward or reversed bias mode. In forward bias mode a positive voltage is applied to the p-region and negative voltage to the n-region. The positive voltage will repeal the holes towards the n-region and vice versa the negative voltage will push the electrons towards the p-region. As a result the depletion layer of the junction will narrow and continuous current will begin to flow through the junction.

By applying a positive voltage to the n-region and a negative voltage to the p-region, the p-n junction is operated in the reversed bias mode. The positive voltage in the n-region now attracts electrons towards the positive electrode and the negative voltage attracts holes towards the negative electrode, widening the depletion region as shown in figure 6. The electric field over the depletion region increases as well and prevents the major charge carriers from crossing over the junction, thus no current will flow through the junction. However, an electron hole pair may be created in the depletion region due to thermal excitation or an absorption of a photon. The electric field over the depletion region will then push the electron towards the positive electrode and hole towards the negative electrode, resulting in a net current flowing through the junction. If the electric field over the depletion layer is sufficiently high, the electron and the hole will gain enough kinetic energy to create secondary charge carriers upon collision in a process called impact ionization. The newly created electron-hole pairs will also accelerate due to the electric field allowing further ionization of atoms, resulting in a self-sustaining multiplication process of charge carriers called the avalanche breakdown.

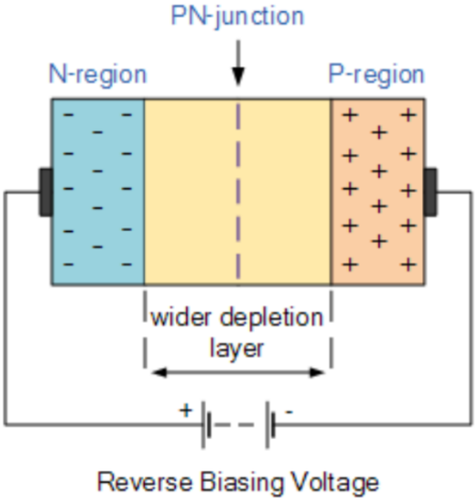

Figure 6: Connecting the p-n junction to reversed bias widens the depletion layer [10].

When the bias voltage over the diode is increased to the point in which the avalanche breakdown starts to happen, the current flowing through the junction rapidly increases. Typical I-V characteristics of a reverse biased p-n junction are shown in figure 7, where the breakdown voltage V_{br} marks the point in which the electric field over the junction is sufficiently high for avalanche breakdown to occur. When a diode is operated above[1] the breakdown voltage it is said to be operated in the Geiger mode.

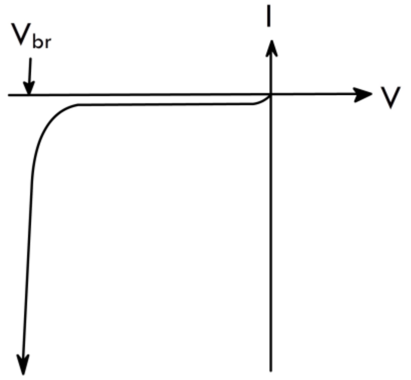

Figure 7: I-V characteristics of a reverse biased p-n junction. The breakdown voltage V_{br} is the minimum voltage required for avalanche breakdown. Above the breakdown voltage the current through the diode increases exponentially.

The breakdown voltage is an important characteristic for diodes as it determines the minimum voltage required to operate them in the Geiger mode. The difference between the bias voltage V_{bias} applied to the diode and the breakdown voltage V_{br} is called the overvoltage

$$\Delta V = V_{bias} - V_{br}. \tag{2}$$

When a diode is used as a photodetector, the applied overvoltage has a strong effect on its properties such as gain, photon detection efficiency and dark count rate, which will be discussed in the later chapters.

---

[1] Here and further on we imply the voltage magnitude, keeping in mind that it is negative, the diode is biased in the reverse direction.

1.3 Single Photon Avalanche Diode

A Single Photon Avalanche Diode (SPAD) is a solid-state photodetector based around a p-n junction operated in the Geiger mode. As shown in the previous chapter, a reverse biased p-n junction will produce a macroscopic current in response to a photon being absorbed in the depletion layer. The high gain from the avalanche breakdown allows light detection on a single photon level, makings SPADs highly sensitive photodetectors.

When a photon triggers an avalanche breakdown, the avalanche needs to be quenched down before a subsequent measurement can be made. This can be achieved through either active or passive quenching. The former relies on a more elaborative active circuit while the latter uses a simple resistor in series with the SPAD. An equivalent circuit of a SPAD [11] with an integrated passive quenching resistor is shown in figure 8. The SPAD is modelled as a parallel connection of the internal resistance R_d of the diode and the capacitance C_d of the inner depletion layer. R_q is the resistance of the quenching resistor and the parasitic capacitance of the resistor is modelled with a parallel capacitance C_q. The combination of the SPAD and the quenching resistor is referred to as a microcell.

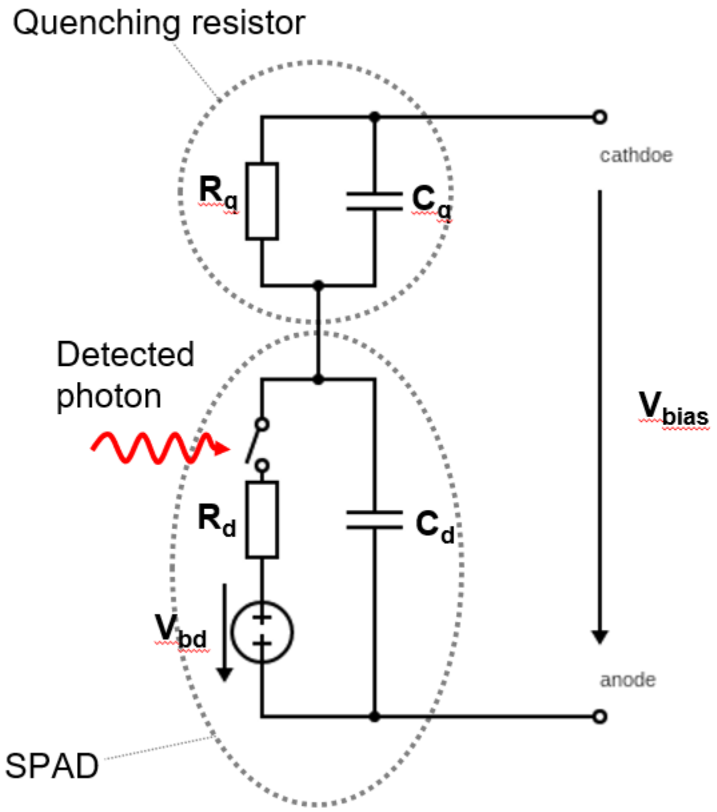

Figure 8: A simple quenching circuit consisting of a SPAD connected in series with a quenching resistor.

When the SPAD is ready to detect a photon the switch in figure 8 is open, C_d fully charged and the node between C_q and C_d is charged at the bias voltage V_{bias} applied to the SPAD. Once an avalanche is triggered, either by a photon or some other even such as a thermal excitation of an electron, it is modelled by closing the switch in figure 8. This will start to discharge capacitor C_d and recharge capacitor C_q, resulting in an exponential potential drop at the node between the two. The discharge of C_d (and recharge of C_q) will stop once the current I_d through R_d reaches the minimum value required for self sustaining avalanche process, which is slightly above the asymptotic minimum value I_{df}, given by $I_{df} = (V_{bias} - V_{bd})/(R_q + R_d)$. Once the avalanche is quenched, the microcell will return to the state with an open switch. C_d will start to charge, and C_q to discharge, through the resistor R_q and the node between the two will charge back to the bias voltage V_{bias}. Once the microcell has recharged above the breakdown voltage, it is ready to trigger again and a subsequent photon can be detected. The breakdown, avalanche, quenching and recharge cycle of a SPAD operated in Geiger mode is illustrated in figure 9.

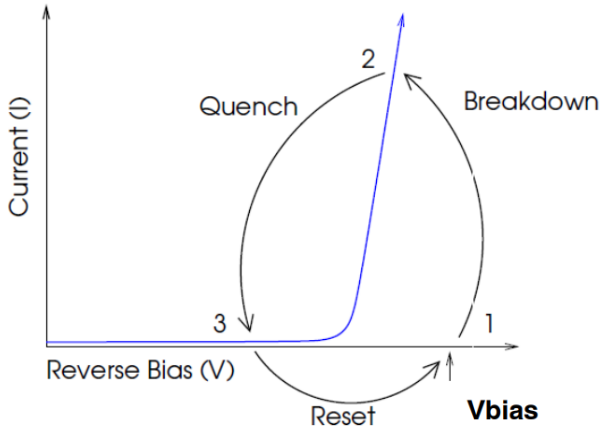

Figure 9: Breakdown, quench and reset cycle of a SPAD operated in Geiger mode [12].

The time it takes for a SPAD to quench the avalanche and reset back to the applied bias voltage is called the recovery time and it determines the count rate of the SPAD. The recovery time

$$\tau_{RC} = C_d(R_q + R_s \cdot N) \tag{3}$$

of a sensor depends on the effective capacitance C_d of the microcell, the quench resistor R_q, any other resistance R_s in series with the sensor and the number of microcells N used in a sensor (for SPAD N=1). The recovery time ranges from tens of nanoseconds up to several microseconds depending on the active area of the microcell. Figure 10 shows a standard pulse shape of a SPAD, where the fast rise time of the pulse is determined by the rise time of avalanche formation and the recovery time by equation (3).

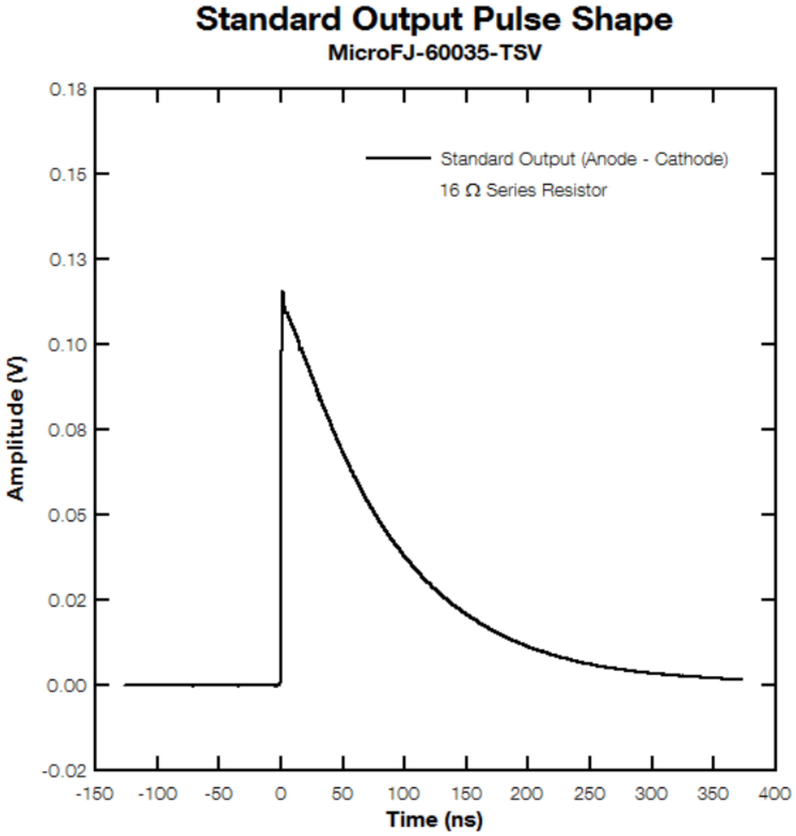

Figure 10: Typical output pulse shape when a single SPAD is fired. Pulse shape measured from a Onsemi MicroFJ-60035-TSV SiPM [12].

The recovery time sets a limit for the photodiode when it is ready for a new measurement. If a photon arrives to the microcell before it has fully recovered the bias voltage, it can still be triggered but with reduced gain due to the lower overvoltage. When the flux of photons is high enough that the microcell fires immediately after recovering pass the breakdown voltage, the photodiode gets saturated resulting in an inaccurate photon count measurements. This limits the applications of SPADs to single photon detectors, as any information of the magnitude of an instantaneous photon flux is lost due to the saturation. To measure the photon flux multiple SPADs are needed and the total flux can be measured by adding together the signals from the individual microcells. This technique has been applied in Silicon Photomultipliers commonly known as SiPMs and will be discussed in the next chapter.

1.4 Silicon Photomultiplier

A Silicon Photomultiplier consists of a dense array of independent SPADs integrated together. Each SPAD is connected in series with its own quenching resistor and is operated in Geiger mode independently. The microcells are connected in parallel with bias voltage applied over them. Figure 11 shows a simplified circuit of an Onsemi SiPM, where in addition to the quenching resistor additional capacitors for fast output are present in the microcell. The fast output is a modification developed by Onsemi for ultra-fast timing measurements. The measurements for this thesis were done using the standard output and thus the fast output will not be discussed any further.

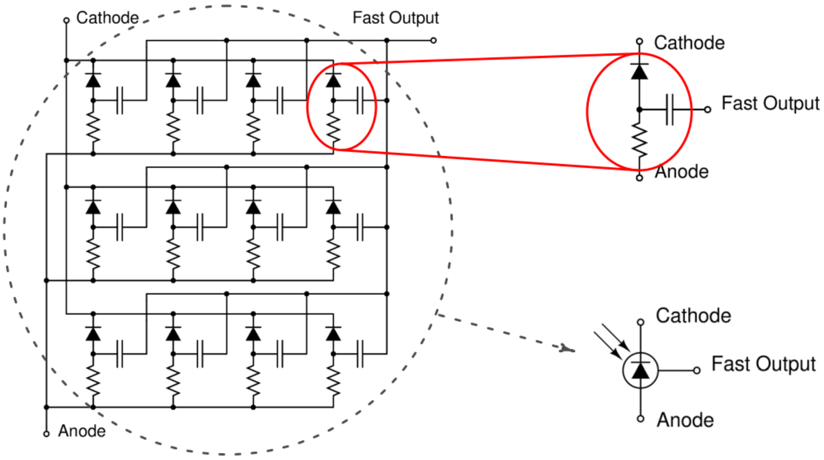

Figure 11: Simplified circuit of an Onsemi SiPM consisting of an array of microcells. Each microcell contains a SPAD, quenching resistor and a fast output capacitor [12].

Now each microcell in a SiPM is capable of detecting photons as described in the previous chapter. When a microcell is triggered by a photon, the following avalanche will be contained only in that microcell[2] while all the other microcells remain fully charged and ready to detect photons. If multiple photons arrive at different microcells simultaneously, they will all react independently and produce identical photocurrents in response. The total current through a SiPM is the summed output of all these microcells, forming a quasi-analog signal. SiPMs are thus capable of measuring the magnitude of an instantaneous photon flux. Figure 12 shows the discrete nature of the SiPM output signal, where each photoelectron (p.e.) created in a microcell results in a similar output pulse. Multiple microcells triggering simultaneously result in a higher p.e. pulse. By increasing the number of microcells N in a SiPM, a larger photon flux can be measured, but the recovery time of the sensor increases according to (3). The number of microcells in a SiPM ranges from hundreds to tens of thousands, depending on the preferred properties.

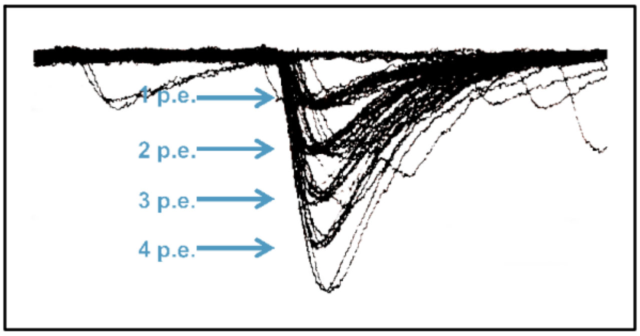

Figure 12: Discrete nature of the SiPM output when illuminated by low-level light pulses. Pulse height corresponds to the number of photoelectrons (p.e.) generated [12].

The pulse shape of a single microcell (see fig. 10), and therefore the output pulse of the SiPM (fig. 12), depend on the gain of the microcell. The gain G is defined as the amount of charge created for each detected photon event and can be calculated

---

[2] The initial avalanche might, however, trigger secondary avalanches in the neighbouring microcells in an effect called cross-talk, which will be discussed in more detail later.

as the ratio of the charge generated from an activated microcell to the charge of an electron. The total charge Q generated by an event is

$$Q = N_{fired} \cdot G \cdot q \tag{4}$$

where N_{fired} is the number of triggered microcells and q the electron charge. The total charge is equal to the integral of the photocurrent pulse and can be used to numerically solve the gain. If the microcell capacitance C is known, the gain can also be given as a function of overvoltage ΔV

$$G = \frac{C \cdot \Delta V}{q}. \tag{5}$$

The applied overvoltage thus changes the pulse shape, with an increase in overvoltage resulting in higher peaks.

The photon detection efficiency (PDE) of a SiPM is the statistical probability that an incident photon triggers a microcell and produces an avalanche. The PDE is defined as

$$PDE(\lambda, V) = \eta(\lambda) \cdot \epsilon(V) \cdot F, \tag{6}$$

where $\eta(\lambda)$ is the quantum efficiency of silicon, $\epsilon(V)$ the probability for a created charge carrier to trigger an avalanche and F the fill factor of the sensor. Each microcell requires some space for a quench resistor, signal tracks and for optical and electric isolation, thus resulting in some inactive area on the sensor surface. The fill factor is simply the relation of the active area to the total area of the SiPM.

The quantum efficiency is defined as the number of charge carriers generated per incident photon. The quantum efficiency can be calculated from the photogenerated current I_p and incident optical power P_{opt} as

$$\eta = \frac{I_p}{q} \cdot \left(\frac{P_{opt}}{hv}\right)^{-1}, \tag{7}$$

where q is the charge of an electron and hv the photon energy of wavelength λ. The first term is effectively the number of charge carriers created and the second is the inverse of the number of incident photons. The quantum efficiency, and hence the PDE, strongly depend on the wavelength as shown in figure 13. With different designs of the sensor the peak PDE wavelength can be changed. The electrons have a higher probability of initiating an avalanche than the holes, thus better efficiency can be achieved when the initial photon interacts in the p-region. This maximizes the flow of electrons through the high electric field where an avalanche can be triggered. With a p-on-n structure the sensor will be more sensitive to shorter wavelengths and with an n-on-p structure a better sensitivity to longer wavelengths can be achieved.

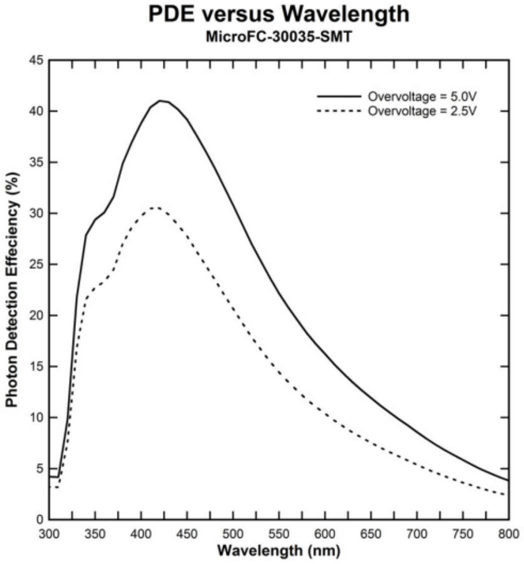

Figure 13: PDE as a function of wavelength for different overvoltages. Data reported by Onsemi for a MicroFC-30035-SMT SiPM [12].

The avalanche initiation probability $\epsilon(V)$ takes into account that some charge carriers might recombine or not gain enough kinetic energy to trigger an avalanche. As the kinetic energy gained by the charge carriers depends on the electric field strength over the depletion region, the avalanche initiation probability is a function of the overvoltage. The PDE as a function of bias voltage for an Onsemi SiPM is shown in figure 14.

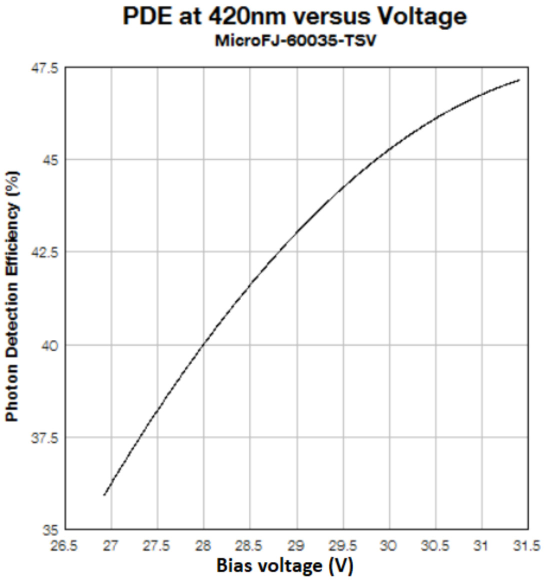

Figure 14: PDE as a function of bias voltage for Onsemi MicroFJ-60035-TSV SiPM [12].

The PDE can be determined with the help of the responsivity R of the photodiode. The responsivity is defined as the generated photocurrent I_p per incident optical power P_{opt}:

$$R = \frac{I_p}{P_{opt}}. \tag{8}$$

With the definition of the quantum efficiency (7) it can be given as

$$R = \frac{\eta q}{hv} = \frac{\eta q \lambda}{hc}. \tag{9}$$

Then taking into account the internal gain G, afterpulsing probability P_{AP} and crosstalk probability P_{XT} (which will be discussed in more detail later), the PDE can be determined from the relation

$$PDE = \frac{R \cdot h \cdot c}{\lambda \cdot G \cdot q \cdot (1 + P_{AP}) \cdot (1 + P_{XT})}. \tag{10}$$

While increasing the overvoltage has a positive affect on the PDE as shown in figure 14, it also increases the noise of a SiPM. The main source of noise in a SiPM, when excluding any external contributions such as incident light, are thermally generated electron-hole pairs, referred to as dark counts. The dark count rate (DCR) depends on the active area of the sensor, the applied overvoltage and the temperature. The response of a SiPM to either a photon-generated or thermally-generated electron-hole pair is identical, thus the dark counts cannot be excluded from the signal and cause noise on a single photon level. The typical DCR at room temperature is of the order of 100 kHz/mm^2 [13] and will result in a macroscopic dark current. By cooling the SiPM the dark count rate can be suppressed rapidly as for every 10 K reduction in device temperature there is a 50 % decrease in the DCR [12].

An additional component of noise is created by the optical crosstalk between neighbouring microcells. When an avalanche is triggered in a microcell, the accelerated charge carriers will emit photons which in turn might initiate secondary avalanches in neighbouring microcells. The probability for this to happen is the crosstalk probability P_{XT}, which is proportional to the overvoltage. This imposes an inherent trade off between the PDE and the noise caused by crosstalk. The secondary avalanches caused by crosstalk happen almost instantaneously [14] and appear as higher peaks in an oscilloscope shot. In figure 15 is shown a single dark count and double dark count resulting from crosstalk. The time difference between two subsequent dark counts is exponentially distributed [15] and the probability of detecting two dark counts as a single event requires them to occur in a sub-nanosecond time window, and is of the order $p \sim 1 - e^{-1\ \mathrm{ns}\cdot 1\ \mathrm{MHz}} < 0.01\ \%$ for a DCR of 1 MHz. The crosstalk probability is many orders of magnitude higher [13] and therefore it is the primary contributor to the double peaks appearing. Due to the practically instantaneous nature of crosstalk the rise time of the signal is not affected.

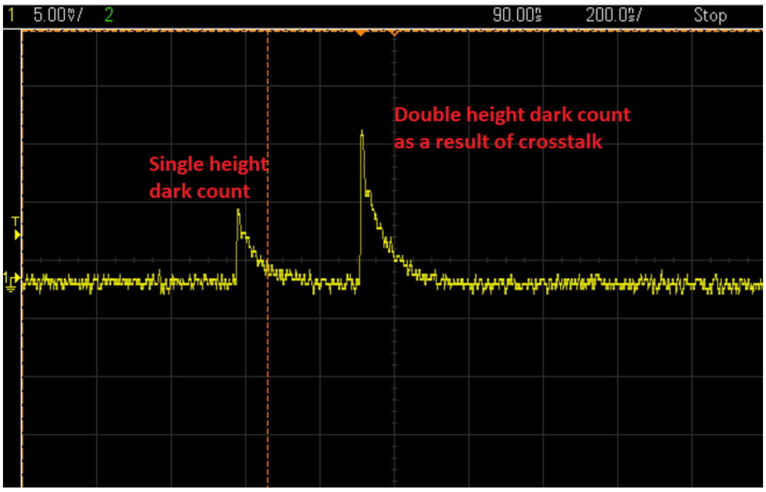

Figure 15: Oscilloscope shot showing a single dark count and dark count with crosstalk.

A second source of correlated noise in a SiPM is afterpulsing. The deviations of the silicon lattice from the perfect crystal structure are called imperfections or defects and they may introduce new levels into the energy band gap. During the breakdown some carriers can be trapped in these defects for several nanoseconds and then be released, potentially initiating a secondary avalanche in the same microcell. As discussed earlier, if the microcell fires before it has fully recharged, the gain is reduced resulting in a lower output signal. Thus the afterpulses with short delay tend to have negligible impact. When the delay of the afterpulse is of the order of tens of nanoseconds, the microcell has recovered most of the overvoltage and will result in a noticeable noise. Figure 16 shows a dark count with afterpulse occurring 25 ns after the initial breakdown. The microcell has only partially recharged its bias voltage resulting in a lower peak. If the afterpulse were to occur after the microcell has fully reset, it would be indistinguishable from a regular dark count. The afterpulsing probability depends on the overvoltage and is less than 5 % in the normal operation range [13].

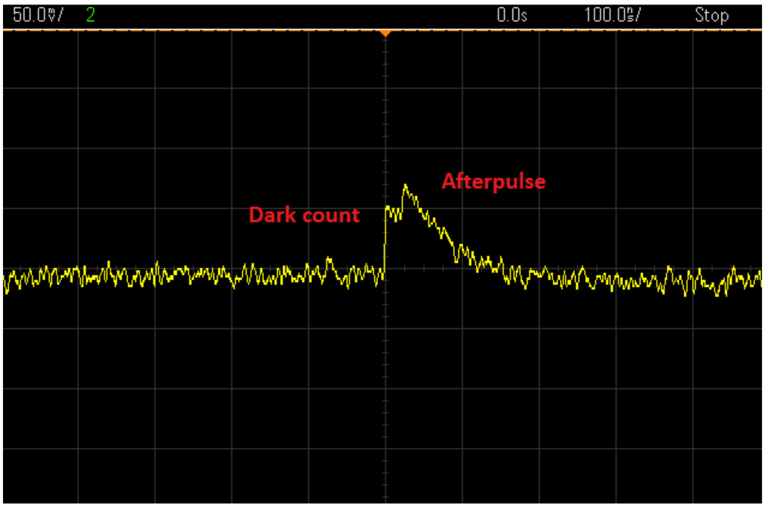

Figure 16: Oscilloscope shot showing a dark count with afterpulse.

The properties of SiPMs at room temperature are well understood and documented, but the understanding of SiPM behaviour at cryogenic temperatures mainly relies on the results of a few recent experiments. Since many of the parameters depend on the design of the SiPM, these results cannot be generalized for all SiPMs. However, the underlying properties of silicon can be studied to make generalized predictions for SiPMs. In the next chapter the effects of temperature on silicon and SiPMs will be discussed, both based on theory and experimental reports.

1.5 Silicon Photomultiplier at cryogenic temperatures

As shown in the previous chapter, the applied overvoltage ΔV has a major impact on the properties of a SiPM. As the overvoltage is defined as a function of bias and breakdown voltages (equation (2)), the temperature effects on the breakdown voltage need to be taken into consideration.

In the room temperature region the breakdown voltage changes linearly as a function of the temperature [12] and the linear behaviour has been reported to continue down to 77 K for some detectors [16] while for others the linear temperature coefficient started to decrease around 150 K and no further changes in breakdown voltage was observed from 77 K to 0.2 K [17]. There also exist reports where the breakdown voltage decreased to a minimum value at 77 K and then increased when further cooled down to 4 K [18]. The discrepancy can be explained by the different doping levels of the sensors and its effect on the charge carrier mobility.

For the avalanche breakdown to occur the charge carriers require sufficient kinetic energy for impact ionization. The drift velocity of charge carriers in an electric field depends on their mobility μ, which in turn is affected by the different scattering phenomena in a semiconductor crystal. The most important scattering mechanism is related to the lattice vibrations of the crystal, called phonons. In figure 17 is shown how the charge carrier mobilities change as a function of temperature due to phonon scatterings. The increase in carrier mobility explains the shared linear behaviour of breakdown voltage for different sensors.

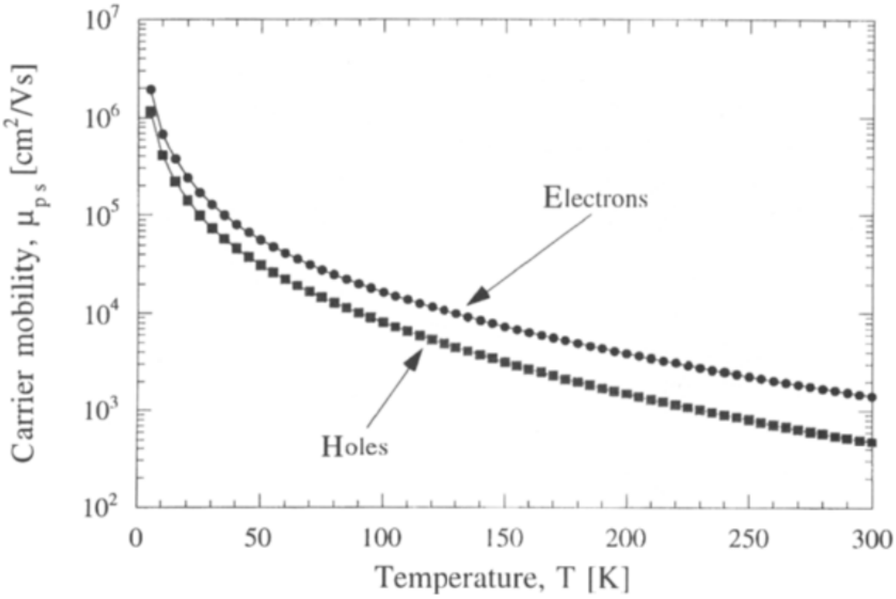

Figure 17: Temperature effect on electron and hole mobilities due to phonon scattering [7].

The discrepancies in lower temperatures start to arise when taking into account other scattering mechanisms, such as the impurity, carrier-to-carrier and surface scatterings. Figure 18 shows the calculated total effective electron mobility for different doping concentrations. The electron mobilities change linearly as a function of temperature from room temperature to around 70 K, after which discrepancies start to appear. The difference in behaviour of sensors upon cooling can be explained with different doping concentrations.

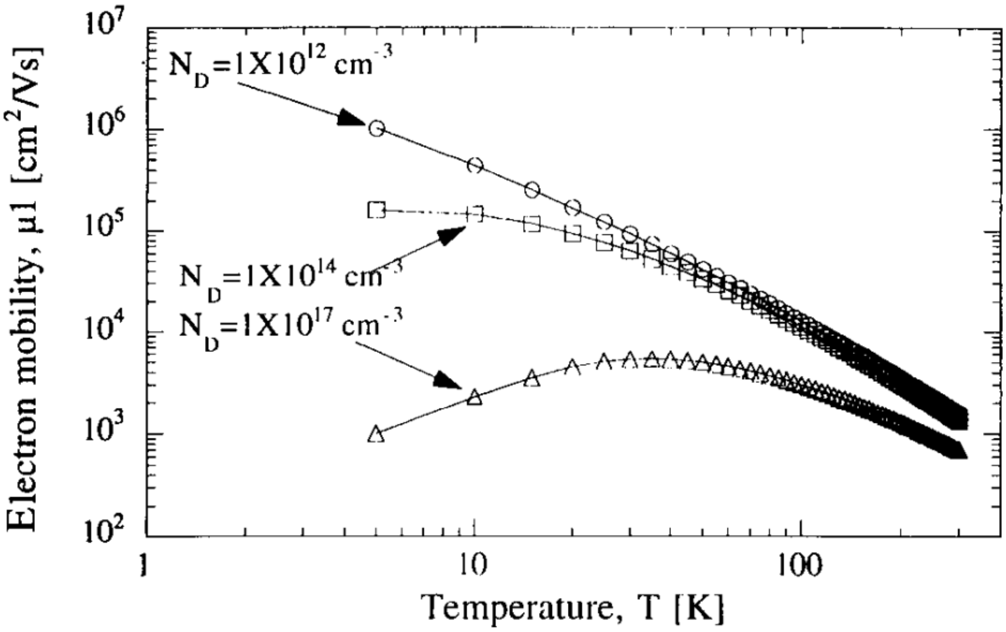

Figure 18: Calculated total electron mobility for three doping levels [7].

The changes in PDE due to temperature are quite complex, as different counteracting mechanisms are expected to effect the PDE [19]. The main factors effecting the PDE are the changes in avalanche triggering probability $\epsilon(V)$, absorption coefficient α and carrier freeze-out. The avalanche triggering probability increases due to enhanced carrier mobility and figure 18 can be used to estimate the changes in PDE as a function of temperature. The absorption coefficient affects the quantum efficiency $\eta(\lambda)$ of the sensor and is reduced due to the widening of energy gaps at lower temperatures, resulting in a lower PDE. At temperatures below 120 K (kT $\approx$ 0.01 eV) the thermal energy is no longer sufficient to ionize the doped impurity atoms resulting in a reduced charge carrier concentration in a phenomenon called carrier freeze-out, which will further reduce the PDE. The first two mechanisms explain the observed fluctuations [17, 19] in PDE at higher temperatures, while the carrier freeze-out explains the sudden drop below 120 K. The PDE has been reported to reduce by a factor of 3 [18] all the way down to a factor of 10 [8] for different sensors. Despite the reduced PDE the sensors were still capable of detecting single photons.

As mentioned before, the main source of noise in a SiPM is caused by dark counts. In addition to dark counts some noise will be caused by external contributions to the carrier generations such as incident light, IR-radiation or cosmic rays. These sources do not qualify as dark counts since the avalanche is triggered by a photon or a charged particle in each case. However, since it is impossible to differentiate external events from dark counts just based on the output signal and the dark counts are the dominating source of noise, the two will be combined under the same discussion of dark counts.

At room temperature the dark counts are mainly caused by thermally generated electron-hole pairs. When a SiPM is cooled down the dark count rate decreases rapidly, as the thermal energy is no longer sufficient to create electron hole pairs, and below 200 K the dark counts are dominated by band-to-band tunneling [20]. Experimental results show strong suppression of dark counts at low temperatures [18, 19], with the dark count rate reaching as low as 10 Hz at liquid helium temperature.

The correlated sources of noise, crosstalk and afterpulsing, are also affected by the temperature. The reports on crosstalk probability P_{XT} are somewhat conflicting, as there are reports of P_{XT} decreasing [8] and increasing [21] by a factor of three, as well as no observed changes [19] for different temperatures. While P_{XT} is proportional to the avalanche triggering probability, which is temperature dependent, it is clear that there are some additional mechanisms affecting the crosstalk probability which are not yet well understood.

The afterpulsing probability P_{AP} has been reported to increase rapidly below 100 K [19] reaching a saturation point in the 20 K - 40 K region [17, 21], where the dark current due to afterpulsing makes the sensor practically non-operational. When further cooled down below 20 K the P_{AP} dropped and operation became possible again. The increase in P_{AP} is likely due to new charge carrier trapping and release mechanism becoming available, which are related to the carrier freeze-out [19]. Below 20 K the increasing trapping time of charge carriers results in larger delays in afterpulsing, thus lowering the noise.

2 Experimental setup

A dilution refrigerator based test setup is used to characterize the properties of a MicroFJ-30035-TSV SiPM from Onsemi at room temperature and various cryogenic temperatures. We used a homemade dilution refrigerator of atomic hydrogen group of the Wihuri Physical Laboratory, Department of Physics, University of Turku. The dilution refrigerator has nominal circulation rate of 250 μmol/sec and can reach bottom temperatures of 20 mK. Due to the residual heat load from optical feedthrough and coax cables, in this tests we could reach 80 mK at the mixing chamber and cool the board with the SiPM down to 180 mK.

For the measurements the SiPM chip was soldered on a biasing and readout board as shown in figure 19. The biasing and readout board contains low-pass filters for the biasing voltage and a 50 Ω output resistance. The SiPM chip was soldered to the board with small diameter ($d = 0.1$ mm) copper wiring to avoid damage due to the different thermal expansion of the board and the chip. The output signal is connected with a SMA connector. The board was equipped with a ruthenium oxide (RuO2) and a platinum (Pt) thermometer to accurately measure the temperature at different ranges. Below 1 K the temperature could be measured with a precision of

10 mK. Additionally a ruthenium oxide heater was included in the board to control the temperature.

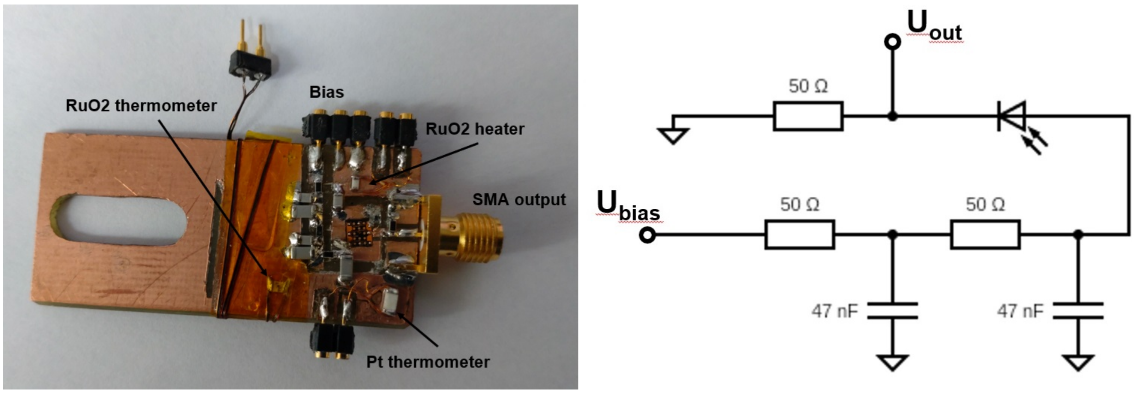

Figure 19: Left: A photograph of the SiPM biasing and readout board. Right: SiPM biasing and readout board circuit diagram.

The SiPM board was placed on top of the mixing chamber inside the dilution refrigerator. Both the bias and SMA output were connected with 0.5 m long semi-rigid coper-nickel coaxial cables with 1.6 mm outer diameter from the SiPM board to the vacuum can flange of the dilution unit (DU). The cables were thermally anchored to the mixing chamber, "0.1 K plate", 0.6 K pot and still (DU components) to avoid any excess heat load. From the vacuum can flange of the DU to room temperature a coper-nickel coaxial cable of length 1.5 m and outer diameter of 2.2 mm was used. A schematic of the dilution refrigerator setup is presented in figure 20. A 275 nm UV LED from Würth Elektronik was mounted on top of the cryostat in a light tight brass mount. A vacuum tight glass window connected to the top end of a stainless steel tube, with the other end connected to the vacuum flange of the DU, was used as a light guide. A rotatable shutter was placed inside the vacuum can to block any thermal radiation coming from room temperature to allow for accurate dark count measurements.

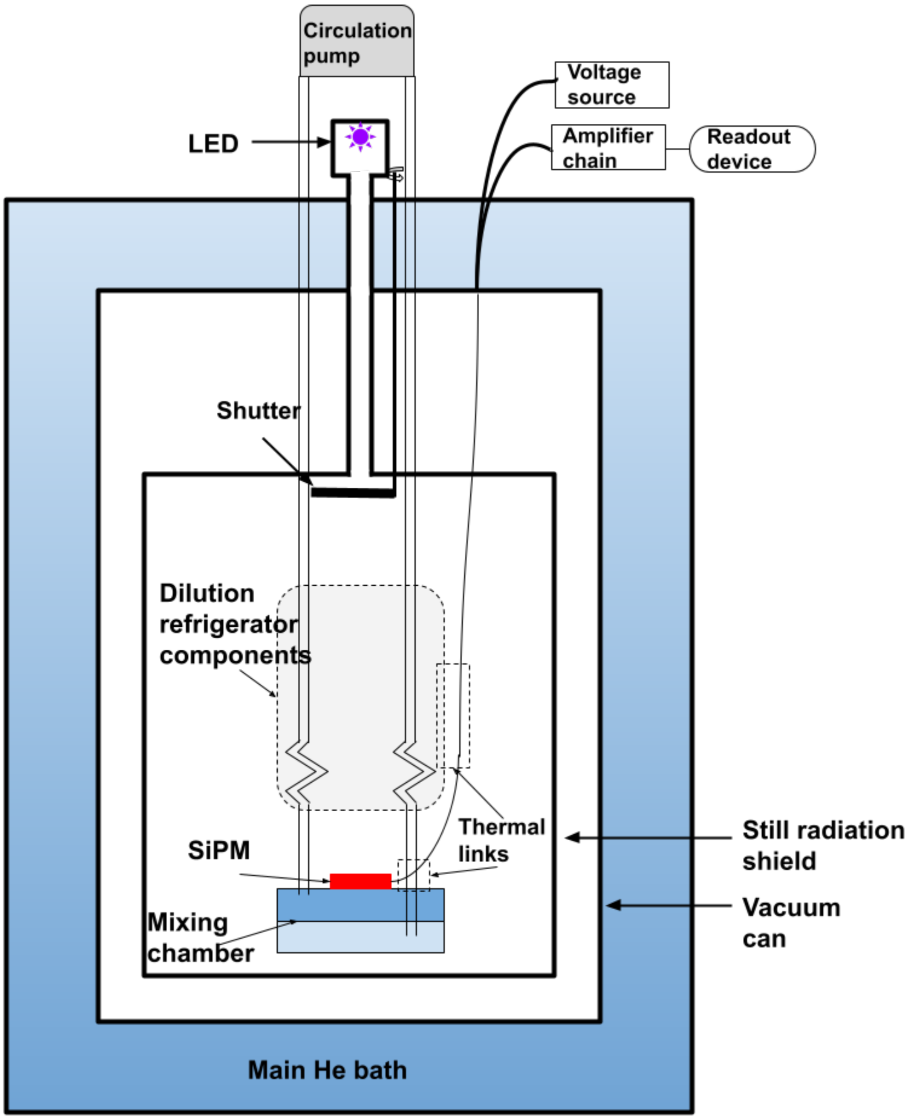

Figure 20: A schematic picture of the dilution refrigerator and test setup used for SiPM characterization at different temperatures.

For the bias voltage and current measurements a programmable Keithley 6487 voltage source was used. The output signal from the SiPM was connected to an amplifier chain consisting of a ZFL-1000NL and a ZFL-1000NL+ amplifiers, both connected to a 15 V DC voltage source resulting in a 23.5 dB gain from each amplifier. The output signal was then read using a Keysight DSOX1102G oscilloscope. Device control, data acquisition and analyse was performed with Python. All relevant programs and raw data are publicly available at a GitHub repository of the author [22].

3 Experimental results

3.1 Pulse shape

The pulse shape of the SiPM was recorded with a Keysight DSOX1102G oscilloscope at different temperatures. The height of the pulse depends on the overvoltage, amplifiers and number of cells triggered, while the shape of the pulse is not affected and varies only with temperature. The average pulse shape of 1 p.e. pulse at room temperature with 2.5 V overvoltage (left) and comparison of different p.e. pulses (right) is shown in figure 21. The pulse shape is composed of the typical fast rise time of the avalanche followed by exponential decay determined by the recovery time (3), as described in the earlier chapter. From an exponential fit the recovery time was determined to be $\tau_{\mathrm{RT}} = 75.2(5)$ ns.

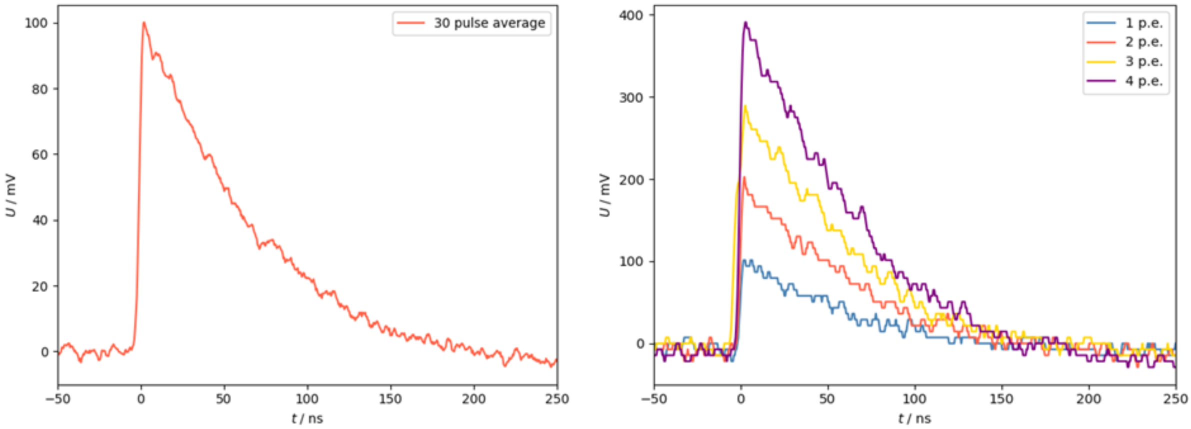

Figure 21: Left: 30 pulse average from 1 p.e. pulses at room temperature. Right: Comparison of different p.e. pulses.

When the SiPM was cooled down to 5.7 K changes in the pulse shape were observed. The fast rise time of the avalanche is not affected, but the recovery time is composed of two distinguishable components; a fast decaying component with a time constant of few nanoseconds to a level of one third of the maximum followed by a slow exponential decay. An average of 30 single p.e. pulses illustrating these two components is shown in figure 22 (left). The differences in pulse shape at cryogenic temperatures are due to an increased quenching resistance resulting in parasitic capacitance in the resistor. The quenching occurs partly due to the parasitic capacitance as modelled in [23]. The recovery time of the slow component shows only minor changes and was $\tau_{5.7\mathrm{K}} = 65.9(11)$ ns. A comparison of different p.e. pulses is presented in figure 22 (right). The discrete nature of the SiPMs signal is not affected and the number of microcells fired is clearly visible in the pulse height.

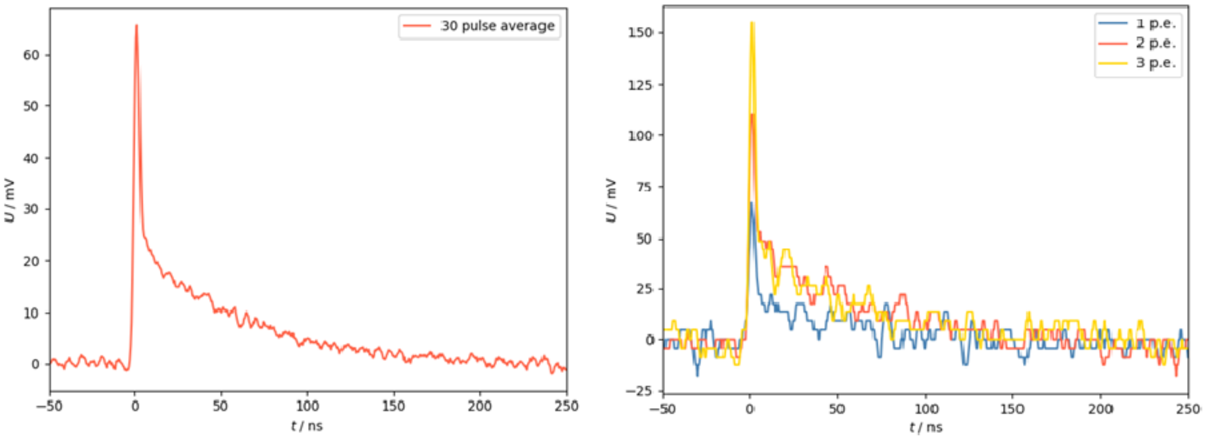

Figure 22: Left: 30 pulse average from 1 p.e. pulses at 5.7 K. Right: Comparison of different p.e. pulses.

To trace the changes of the pulse shape it was measured at four different temperatures. In figure 23 is shown the pulse shape at room temperature, liquid nitrogen and 180 mK. At liquid nitrogen the fast decaying component is already visible with similar time constant of a few nanoseconds down to 80 % of the total pulse height, followed by an exponential decay. Recovery time for liquid nitrogen was $\tau_{\mathrm{LN}} = 137.1(23)$ ns, which was considerably longer compared to other temperatures. At 180 mK the magnitude of the fast component compared to the slow component increases. The recovery time of the slow component was $\tau_{186\mathrm{mK}} = 65.1(13)$ ns. From the recovery times and figure 24 it is evident that the pulse shape and recovery time only show minor changes below 5.7 K.

Changes in the pulse shape and recovery time at sub kelvin temperatures thus have some positive effects on the operation of the SiPM as the recovery time is slightly lower than at room temperature and the sharp peaks of the pulse make it easier to observe single photons with the oscilloscope. However, the measurement of the pulse integral is somewhat more problematic and not as accurate as at room temperature. At liquid nitrogen temperature the recovery time was almost double compared to room temperature, decreasing the maximum photon flux that can be accurately measured.

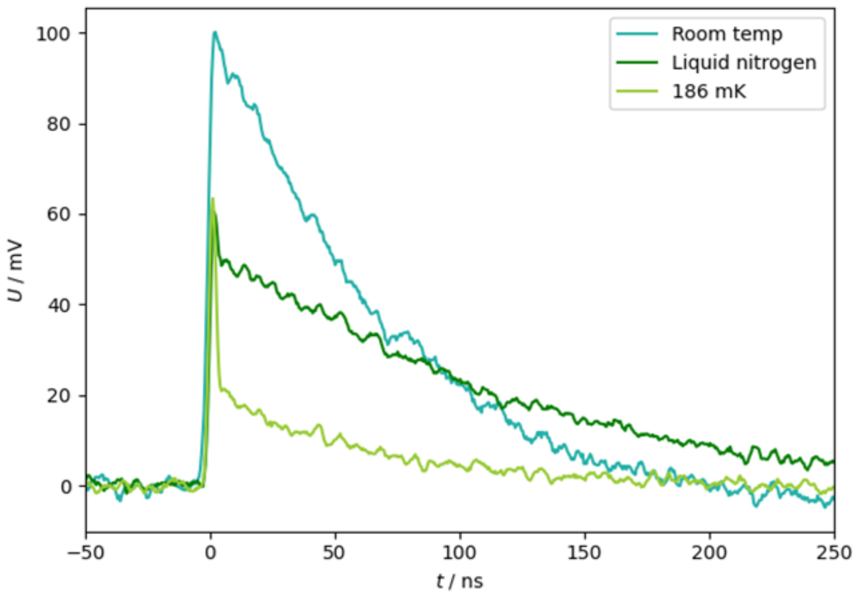

Figure 23: Pulse shapes measured with 2.5 V overvoltage at room temperature, liquid nitrogen and 180 mK, averaged over 30 pulses.

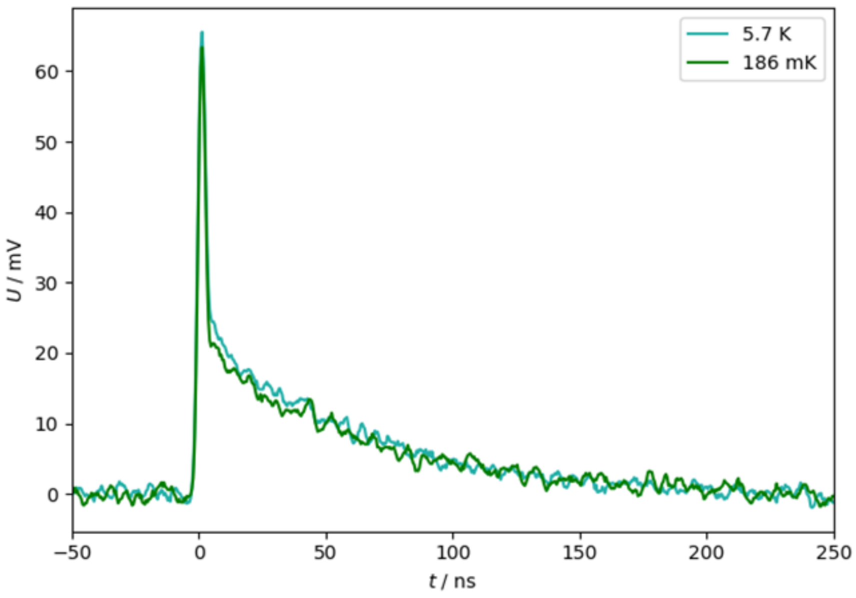

Figure 24: Pulse shapes measured with 2.5 V overvoltage at 5.7 K and 180 mK, averaged of 30 pulses.

3.2 Breakdown voltage

As mentioned in chapter 1, the overvoltage at which the SiPM is operated affects its other properties. As the breakdown voltage depends on temperature it needs to be accurately measured before operating the SiPM at different temperatures. For the determination of the breakdown voltage two different schemes were used. An interception of a linear fit to the $\sqrt{I}$ vs. V, where I is the dark current and V the bias voltage, as presented in [12], and by linear extrapolation of the pulse charge and height to zero, as shown in [8].

The IV-curve of the SiPM was recorded with a Keithley 6487 Source Meter, which was also used to apply the bias voltage. At each bias voltage the average of 10 points was taken to decrease the noise of the device. The $\sqrt{I}V$-curve measured at room temperature is shown in figure 25. The breakdown voltage from the linear fit is $V_{\mathrm{br,RT}} = 24.47$ V.

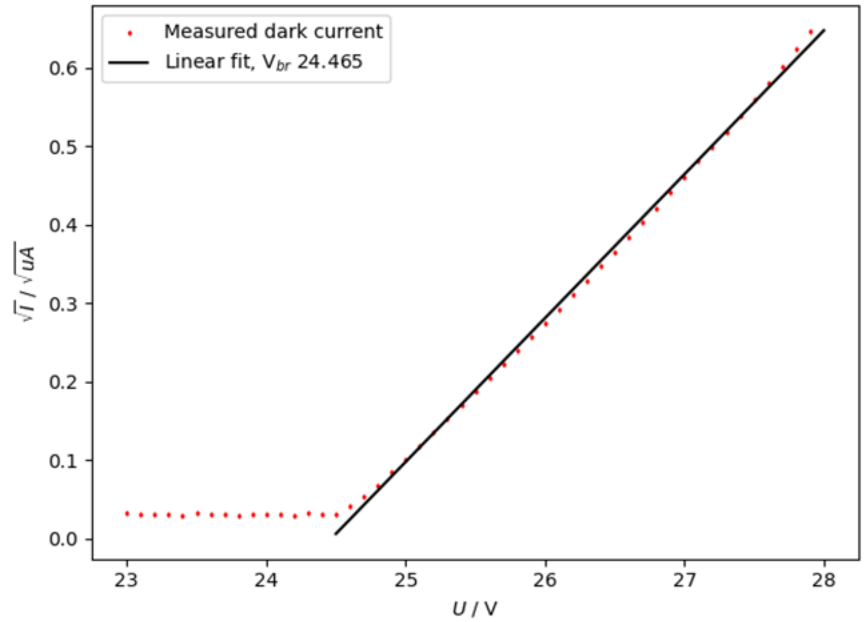

Figure 25: Breakdown voltage determined from the intercept of linear fit to $\sqrt{I}$ vs. V plot at room temperature.

Determining the breakdown voltage from the measured dark current was not possible at cryogenic temperatures due to extremely low dark count rates. Already at liquid nitrogen the dark count rate is too low to measure macroscopic current. Instead the SiPM was illuminated with low intensity UV light from a 275nm UV-LED to replicate the dark current. The measurement results and the linear fit to obtain breakdown voltage of $V_{\mathrm{br,180mK}} = 21.01$ V are presented in figure 26.

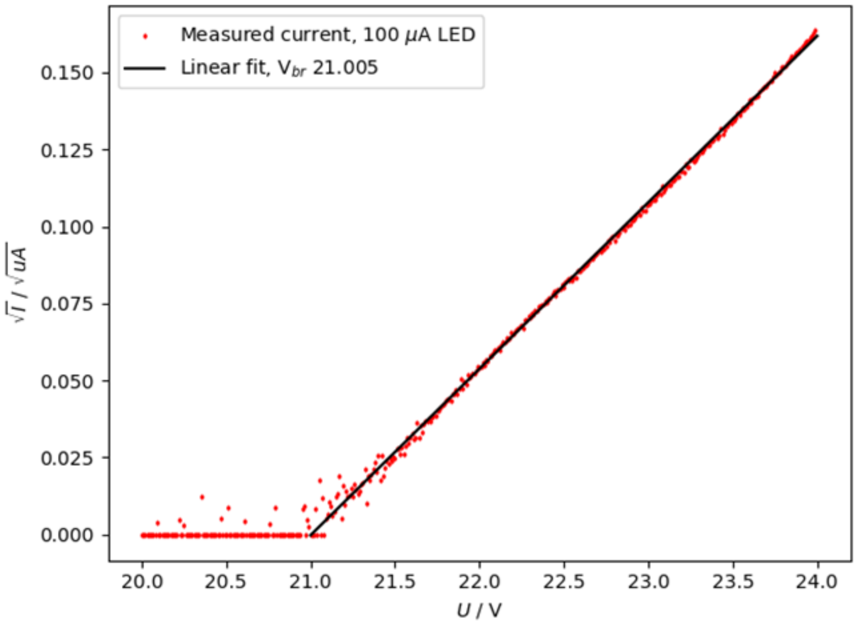

Figure 26: Breakdown voltage measured from the $\sqrt{I}V$-curve with 100 μA UV-LED at 180 mK.

Due to the insufficient dark current at cryogenic temperatures the second method for determining the breakdown voltage was implemented. The pulse height is defined as the maximum amplitude of the pulse with respect to the baseline and the pulse charge as an integral over the pulse waveform

$$Q = \frac{1}{G_{\mathrm{A}} R} \int V(t) \mathrm{d}t, \tag{11}$$

where the voltage gain $G_{\mathrm{A}} = 223.87$ of the amplifiers and resistance $R = 50\,\Omega$ of the circuit have been taken into account.

With the help of a peak filter algorithm 100 single p.e. pulses were recorded with no crosstalk or afterpulsing present as shown in figure 27 (top). Baseline of the pulse was determined from the 450 to 25 ns preceding the trigger and was subtracted from the signal level. From the average pulse form (fig. 27 bottom) pulse height was determined as the maximum amplitude and charge with numerical integral from 0 to 275 ns after the trigger.

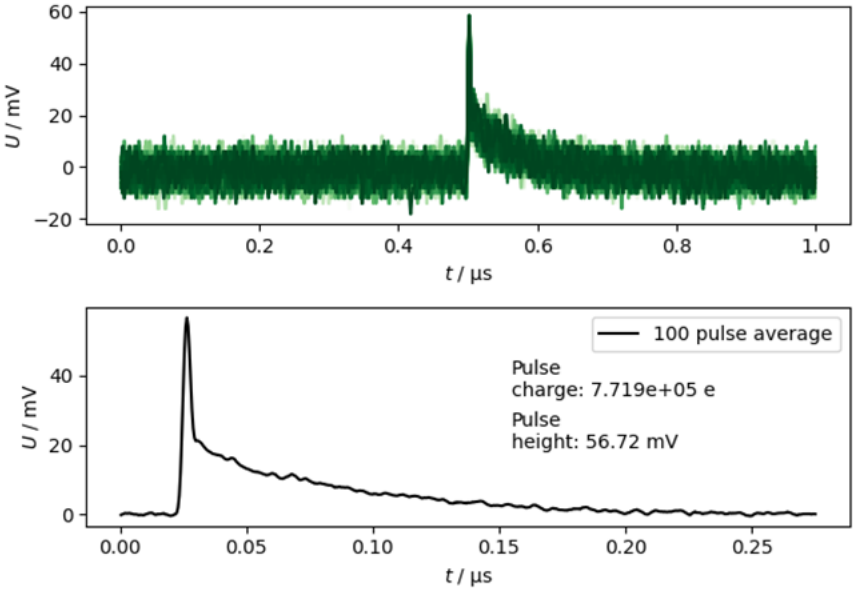

Figure 27: Top: 100 single p.e. pulses recorded with the oscilloscope with 2.5 V overvoltage at 180 mK. Bottom: The average pulse shape, charge from numerical integral of the pulse form and height from the maximum amplitude.

The measurement results for different bias voltages at 180 mK are shown in figure 28, where each point was measured from the average of 100 datasets. The breakdown voltage defined from the pulse charge was $V_{br} = 21.03(14)$ and from the height $V_{br} = 20.84(39)$. The results agree within the uncertainty of the measurement both with each other as well as with the breakdown voltage determined from the $\sqrt{I}V$-curve. The results also confirm that the breakdown voltage can be accurately determined from the IV-curve using a LED instead of the dark current, which is a

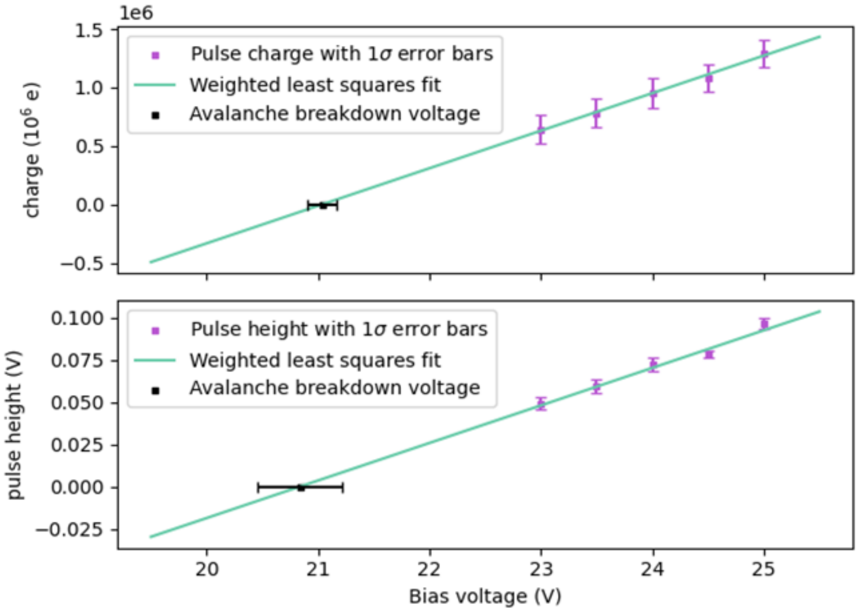

Figure 28: Pulse charge (top) and height (bottom) as a function of bias voltage at 180 mK, measured from the average of 100 datasets. The avalanche breakdown voltage was determined from the linear interpolation to zero. Error bars indicate 1σ standard deviation.

significantly faster method to measure the breakdown voltage at unstable temperatures.

To measure the breakdown voltage as a function of temperature the measurements were repeated at several different temperatures. At stable temperatures, such as room temperature, liquid nitrogen and different points below 7 K, both methods were implemented. Temperatures above liquid nitrogen were measured during the cooling and warming up cycles. Temperatures below liquid nitrogen were stabilised by controlling the cooling power of the dilution refrigerator and by heating the SiPM and mixing chamber with heaters. In figure 29 is shown the measured breakdown voltage as a function of temperature. The breakdown voltage of the SiPM showed similar behaviour as reported earlier [18], reaching a minimum breakdown voltage around 35 K and then increasing at lower temperatures. Below 7 K no further changes in the breakdown voltage were observed. The breakdown voltage shows clear correlation with the electron mobility (see fig. 18) for a high concentration doping.

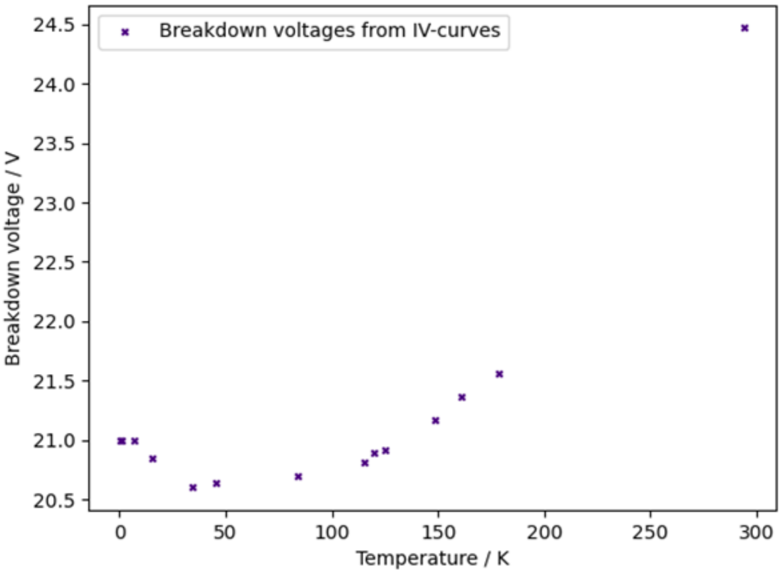

Figure 29: Breakdown voltage measured as a function of temperature.

3.3 Microcell capacitance and gain

The microcell capacitance and gain were determined from the charge vs. bias voltage (fig. 28). The capacitance is defined as

$$C = \frac{Q}{\Delta V} = \frac{Q}{V_{bias} - V_{br}}, \tag{12}$$

corresponding to the slope of the charge Q as a function of bias voltage. The gain can then be calculated from (5) which simplifies to

$$G = \frac{Q}{q}. \tag{13}$$

The microcell capacitances at different temperatures are presented in table I. The total capacitance of the sensor with 5676 microcells in room temperature is 1319 pF, which is roughly 24 % higher than reported by the manufacturer [13]. While the absolute value of the capacitance is quite inaccurate, the changes in capacitance as a function of temperature are consistent with earlier reporting for the same sensor [8], with the microcell capacitance reducing by a factor of 4.1 at 5.55 K compared to room temperature. Below 5 K the capacitance is only slightly reduced and no new behaviour was observed even at the coldest measured temperature of 180 mK.

Table I: Microcell capacitances at different temperatures.

T	Room temperature	Liquid nitrogen	5.55 K	1.09 K	180 mK
C / fF	232.3	195.1	56.49	55.08	51.40

The microcell gain depends on the temperature via the microcell capacitance as well as on the overvoltage according to equation (5). The gain as a function of overvoltage for different temperatures is shown in figure 30. Since the gain is proportional to the capacitance it shows similar reduction at 5.55 K compared to room temperature. The reduced capacitance results in a more gentle incline of the gain as a function of overvoltage. Below 5 K no drastic changes in gain were observed.

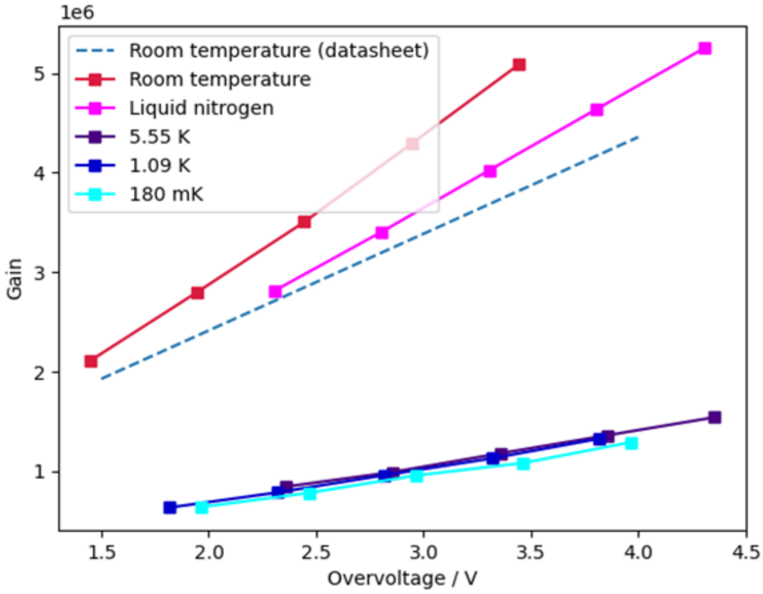

Figure 30: Gain as a function of overvoltage at different temperatures. Comparison to gain at room temperature reported by Onsemi [13].

3.4 Dark count rate and bias voltage operating region

At room temperature the main source of noise is thermally generated dark counts as discussed in chapter 1. The dark count rate rapidly decreases as the temperature is lowered and already at the liquid nitrogen temperature the dark count rate was measured to drop from 50 kHz/mm^2 (for 2.5 V overvoltage at room temperature) down to 20 Hz/mm^2. The dark count rate is further suppressed at sub kelvin temperatures. In figure 31 is shown the dark count rate as a function of bias voltage at 180 mK. For 2.5 V overvoltage the dark count rate is less than one per second.

All the dark count rate measurements were done with the shutter closed. At room temperature there was no difference with open and closed shutter, indicating that the LED mount was light tight. However, at colder temperatures the difference with open and closed shutter was more than an order of magnitude. For example at 180 mK and 3 V overvoltage the dark count rate was 20 Hz with open shutter and 1 Hz with closed shutter. This is believed to be due to the thermal radiation coming from the LED mount which is at room temperature. One can see from figure 31 that the dark count rate with closed shutter slightly increases with overvoltage. The reason for the residual dark count rate at these conditions may be cosmic rays or radiation leaking from room temperature inside the vacuum can of the dilution refrigerator.

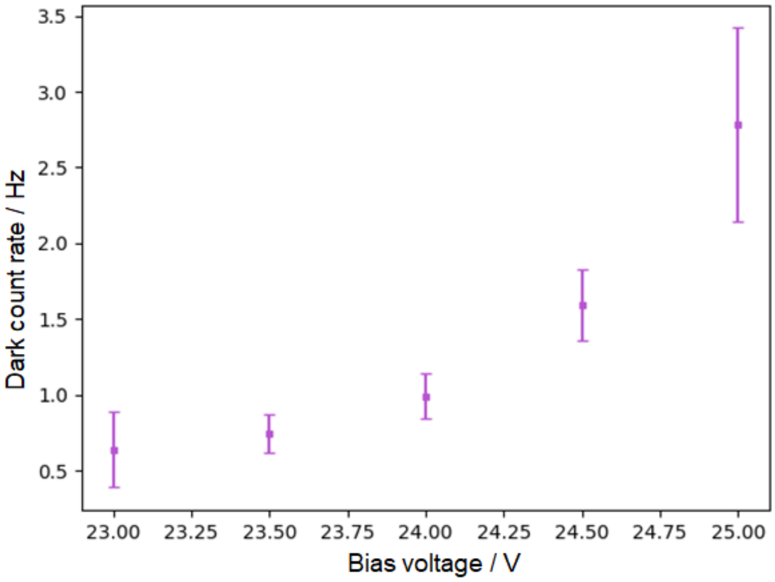

Figure 31: Dark count rate as a function of bias voltage at 180 mK.

At cryogenic temperatures thermally activated dark current is suppressed. However, a quantum tunneling effect through the barrier may allow for the current to flow even at absolute zero temperature. The tunneling can occur via band-to-band tunneling or by trap assisted tunneling. The probability of tunneling increases with stronger electric field and when the field approaches 10^6 V/cm significant current begins to flow through the junction [24]. This increase in dark current due to tunneling was observed as a secondary breakdown where the dark current increased suddenly as a function of bias voltage. The IV-curve measured at 7.5 K is shown in figure 32, where the dark current starts to increase rapidly at 26.55 V. The dark current due to tunneling is clearly distinguishable from the thermally generated dark current as can be seen from comparing figure 32 and figure 33, where the latter is the dark current measured at room temperature. The tunneling effect was observed for temperatures below 40 K, while above 40 K the dark current as a function of bias voltage increased in a similar manner as at the room temperature. The highest applied bias voltage was limited to 36 V to avoid breaking the SiPM.

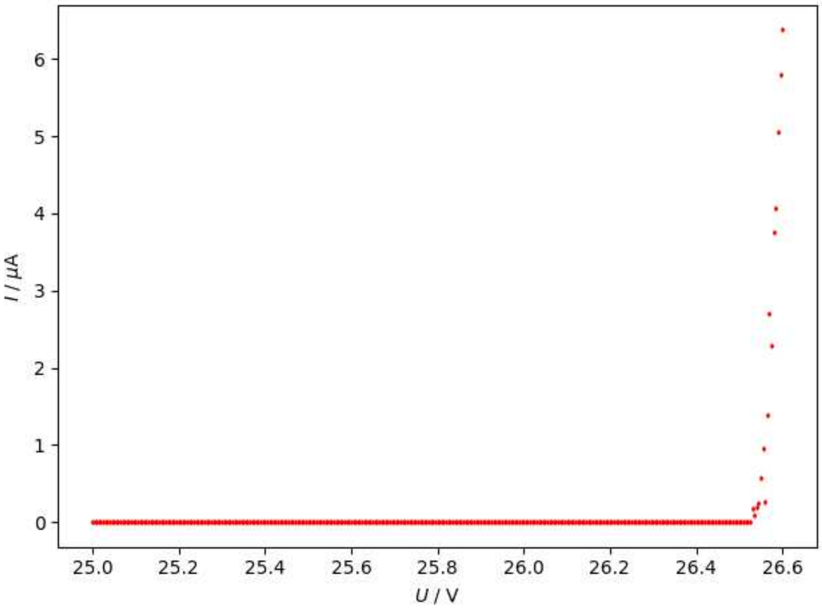

Figure 32: Tunneling breakdown results in a rapid increase of dark current as seen from the IV-curve measured at 7.5 K.

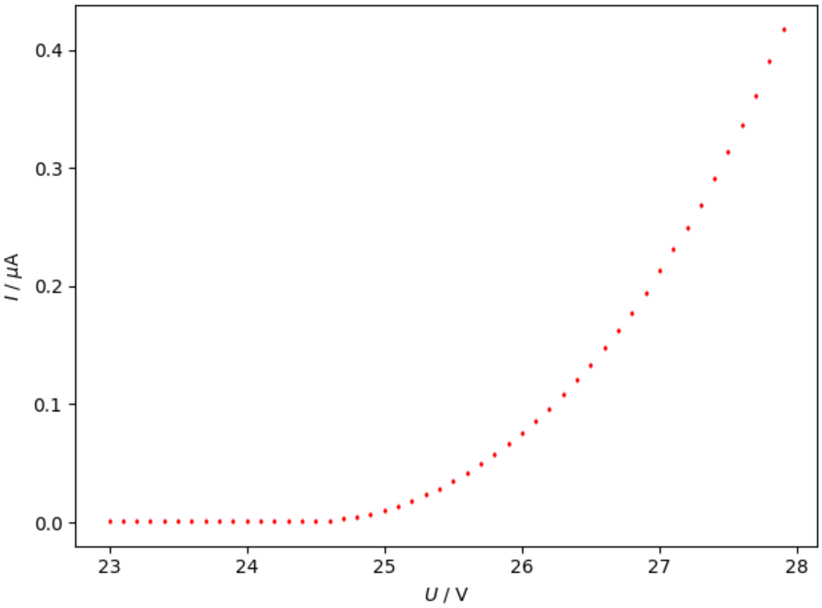

Figure 33: Dark current due to thermal generation of dark counts at room temperature.

Thus, below 40 K, the tunneling breakdown sets an upper limit for the bias voltage at which the detector can be reliably operated. The operating region of the SiPM below 40 K was defined as the voltage range between the avalanche breakdown and tunneling breakdown. In figure 34 is shown the avalanche and tunneling breakdown voltages as a function of temperature. Temperature range between 7 and 77 K is somewhat difficult for a dilution refrigerator for getting stable temperature at a fixed point, as the device is designed for operation well below 1 K. Small cooling power of the fridge can be obtained and regulated by changing the 4He (or 3He) circulation rate, applying heating power with resistive heaters. However, temperatures obtained with this method were not stable and showed some fluctuation during the measurement. The operating region of SiPM decreased down to 25 K and then increased when cooled down further. Below 10 K the operating region stayed stable. Above 40 K the tunneling effect was not observed even at $V_{\text{bias}} = 36$ V, which is considerably higher than the recommended operating voltage by the manufacturer.

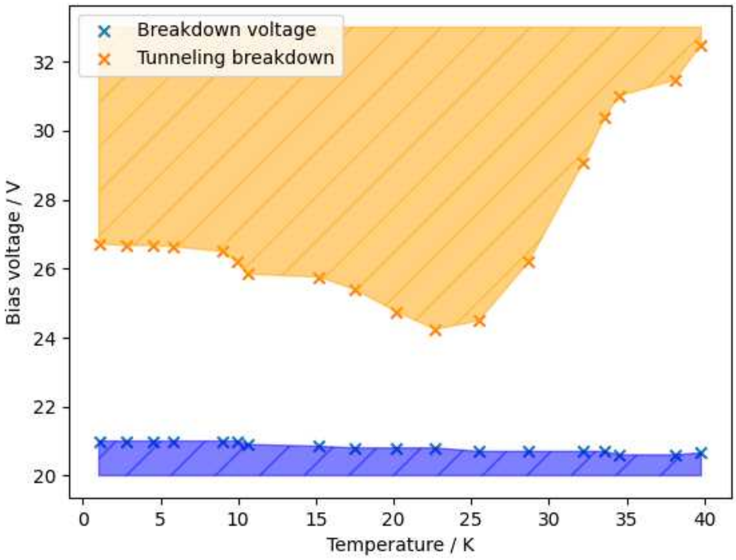

Figure 34: The operating region of the SiPM was defined as the voltage range between the avalanche breakdown and tunneling breakdown.

3.5 Photon detection efficiency and responsivity

The photon detection efficiency has a complex temperature dependence as described in chapter 1.5. Determination of absolute PDE was not possible with the test setup as it would require an integration sphere with a calibrated SiPM. Instead the aim was to measure the relative changes in PDE compared to the PDE at room temperature reported by the manufacturer. For this purpose the SiPM was illuminated with brief low-level light pulses from the UV-LED containing only few photons and the mean number of detected photons λ was determined from the photoelectron distributions. The voltage for the light pulses were generated with a Keysight DSOX1101G oscilloscope wave generator. The same oscilloscope was used to record the waveform of the SiPM with the measurements being triggered synchronously with the applied light pulses. By measuring the average number of photons detected at room temperature and cryogenic temperatures a relation for the PDE could have been established.

However, there were problems acquiring reliable data matching the expected photon statistics at room temperature. Firstly, the oscilloscope was incapable of producing stable pulses to the LED that were short enough to only contain a few photons. At room temperature the shortest stable pulses were containing tens of photons. Secondly, the pulse shape at room temperature (see fig. 21) is not very sharp and thus the resulting signal from such a high number of photons was hard to analyse. Different methods were used to try and determine the average number of photons from each signal, but the results were not consistent and none matched the expected photoelectron distributions.

At 5.7 K and below both of these problems had disappeared. The pulse shape is much sharper (see fig. 22) making it easier to identify single photons from the signal and due to the reduced PDE the average number of photons detected from each pulse was low enough for accurate analyse.

The pulse repetition rate was set to 10 kHz, pulse width to 800 ns and height to 5.5 V. An example of 9 photons detected from a single pulse with 25 V bias voltage is shown in figure 35. Events with crosstalk were counted as single photons and afterpulses happening during the recharge of the microcell were filtered out by adjusting the peak prominence of the algorithm used for counting the peaks. Afterpulses occurring after the microcell had fully recharge could not be distinguished from the signal.

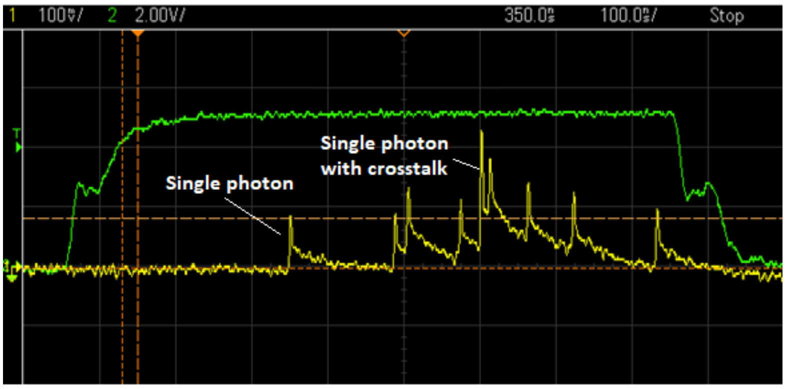

Figure 35: An oscilloscope shot showing 9 photons detected from the LED pulse at 180 mK with 25 V bias voltage.

From each pulse the number of photons was counted, including pulses where no photons were detected. A total of 5000 pulses were recorded and a Poissonian distribution was fitted to the data to get the mean number of photons λ. The measured data with Poissonian fits for two different bias voltages at 1 K is presented in figure 36.

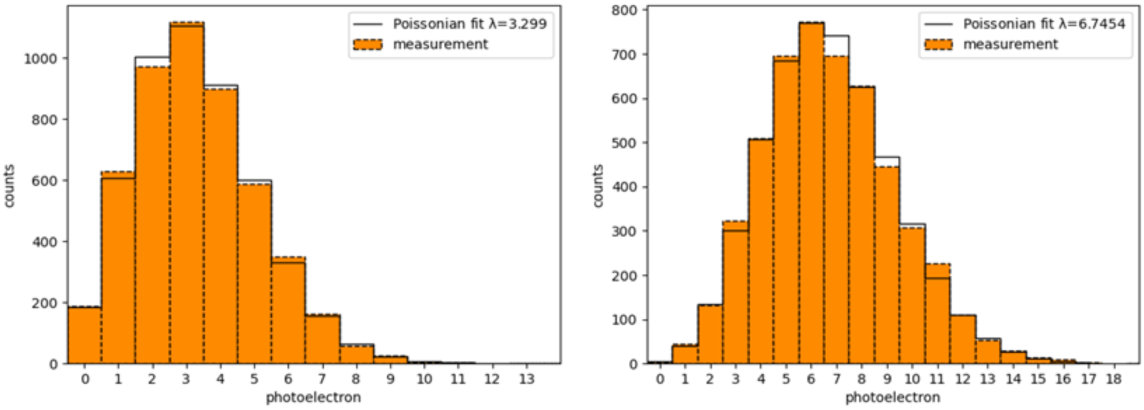

Figure 36: Photoelectron distributions measured from 5000 pulses at 1 K temperature. Poissonian distributions were fitted to get the mean number of photons λ. Left) bias voltage 23.5 V with λ=3.299. Right) bias voltage 25 V with λ=6.7454.

As the absolute PDE could not be determined, the relative PDE was measured as a function of overvoltage instead. 1.5 V overvoltage was chosen as a reference point and the mean number of photons λ at each overvoltage was divided by the reference value. The relative PDE as a function of overvoltage for 1 K and 180 mK temperatures is plotted in figure 37. The relative PDE showed similar behaviour both at 1 K and 180 mK, increasing by a factor of 5 at the highest measured overvoltage. The results are somewhat conflicting with earlier report [8], in which the mean number of photons at 4 K showed only minor increase as a function of overvoltage.

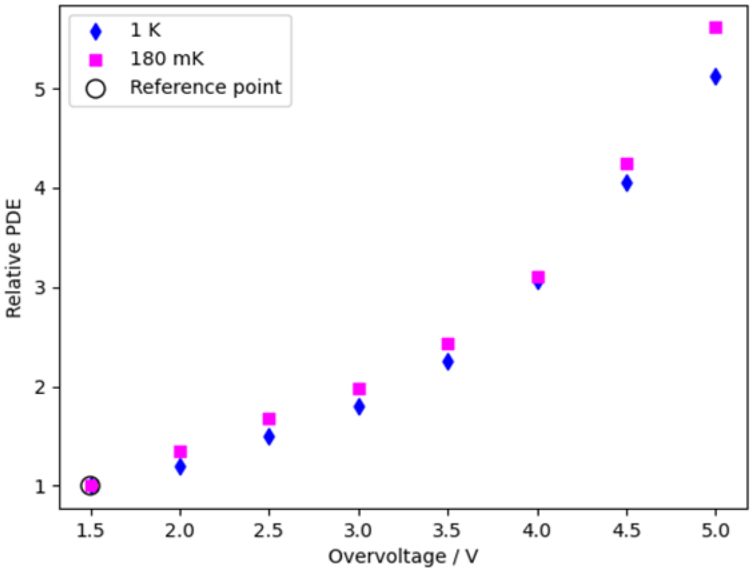

Figure 37: Relative PDE as a function of overvoltage for 1 K and 180 mK temperatures.

The responsivity of a SiPM is defined in equation (8) as the relation of generated photocurrent per incident optical power. The generated photocurrent depends on the PDE according to equation (9) and on the internal gain of the SiPM via (10). Thus an approximation of the PDE can be done by comparing the IV-curves for different LED intensities at different temperatures and taking into account the loss of photocurrent due to reduced gain (see fig. 30). The generated photocurrent was measured as a function of overvoltage for different LED intensities. Results from 1

K and room temperature are plotted in figure 38. The photocurrent was two orders of magnitude smaller at 1 K. Part of the reduced photocurrent is due to changes in the gain, which reduced by a factor of four. Taking this into account, the effective PDE can be estimated to reduce by a factor of 25. The PDE at room temperature at 2.5 V bias voltage for wavelength of 275 nm is 10 % [13], thus the absolute PDE at 1 K is 0.4 %. It should be noted that this method of determining the PDE is not accurate as the generated photocurrent measures the total charge generated in the SiPM, thus the crosstalk and afterpulses increase the photocurrent, and as discussed earlier, both probabilities for crosstalk and afterpulsing increase at room temperature, with the crosstalk probability reducing by a factor of three at 4 K compared to room temperature [8]. The PDE determined from the mean number of photons has been reported to reduce only by a factor of 10 [8].

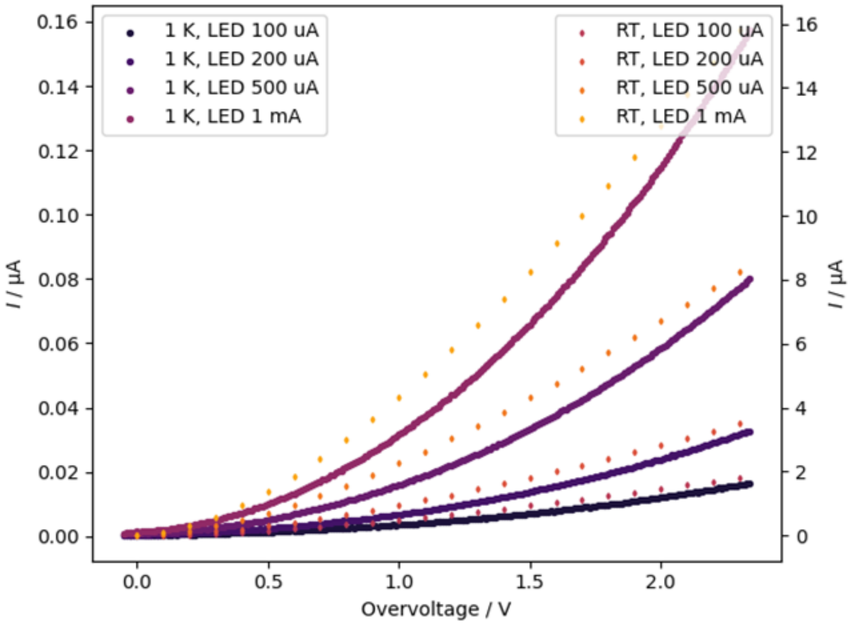

Figure 38: Generated photocurrent as a function of overvoltage for different LED intensities measured at 1 K (left axis) and room temperature (right axis).

The photocurrent was also measured at 180 mK. Comparison of the results at 1

K and 180 mK are plotted in figure 39. The responsivity showed no further decrease and the IV-curves are identical.

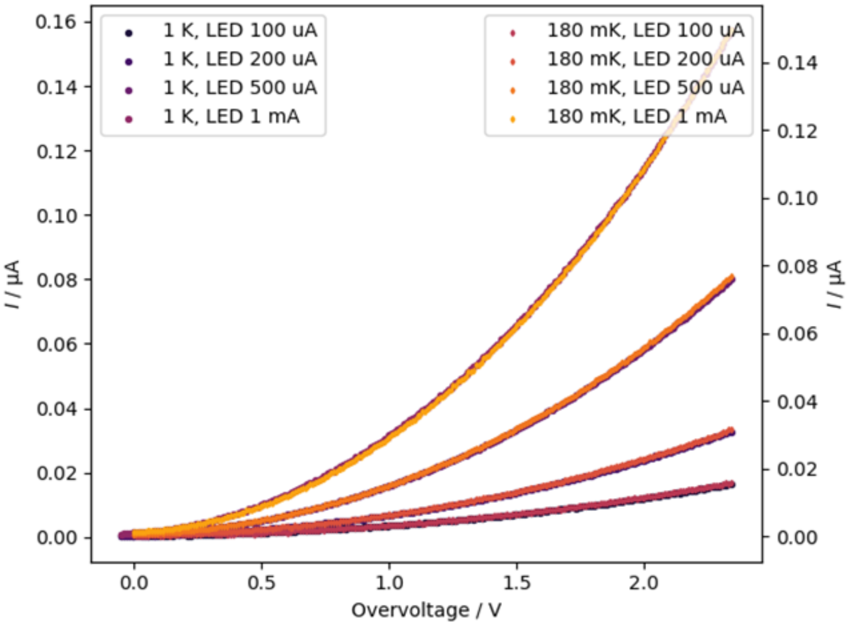

Figure 39: Generated photocurrent as a function of overvoltage at 1 K (left axis) and 180 mK (right axis).

3.6 Thermal cycle damage assessment

A total of two full thermal cycles were done using the same SiPM for all measurements. A comparison of the SiPM characteristics, such as the breakdown voltage, IV-curves, pulse shape and charge, were done at different temperatures during these cycles and no changes were observed.

However, some degradation of the glass covering the SiPM chip was observed when viewed under a microscope as can be seen from comparing figures 40 and 41. The glass covering the SiPM chip had some cracks on it after two thermal cycles. The cracks had mostly formed around the microcells. No reduced performance could be observed. Degeneration tests were not a major focus of our measurements and will be studied in more detail in follow-up measurements.

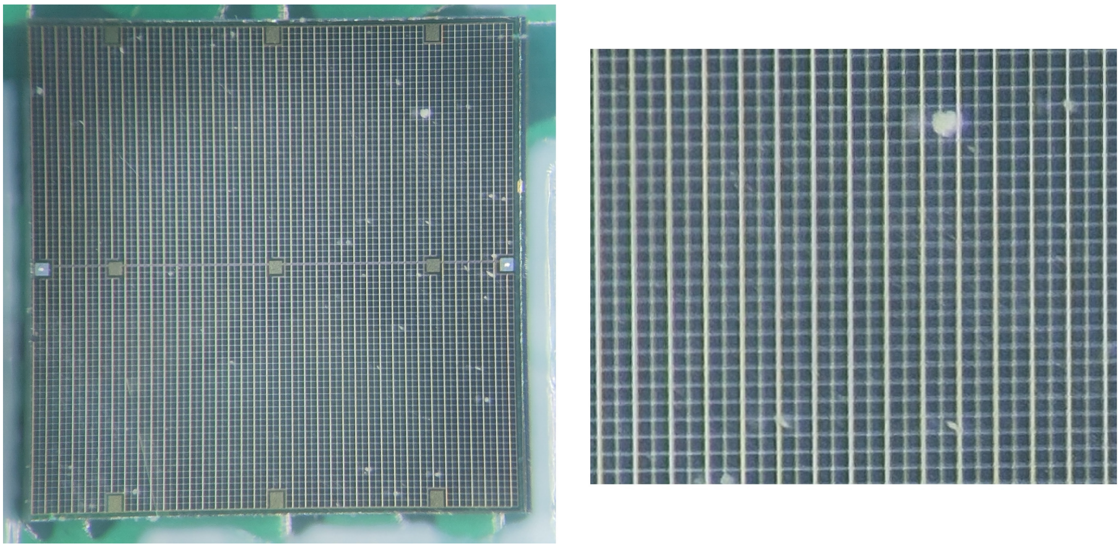

Figure 40: SiPM chip under a microscope before the thermal cycles with a zoomed in image on the right.

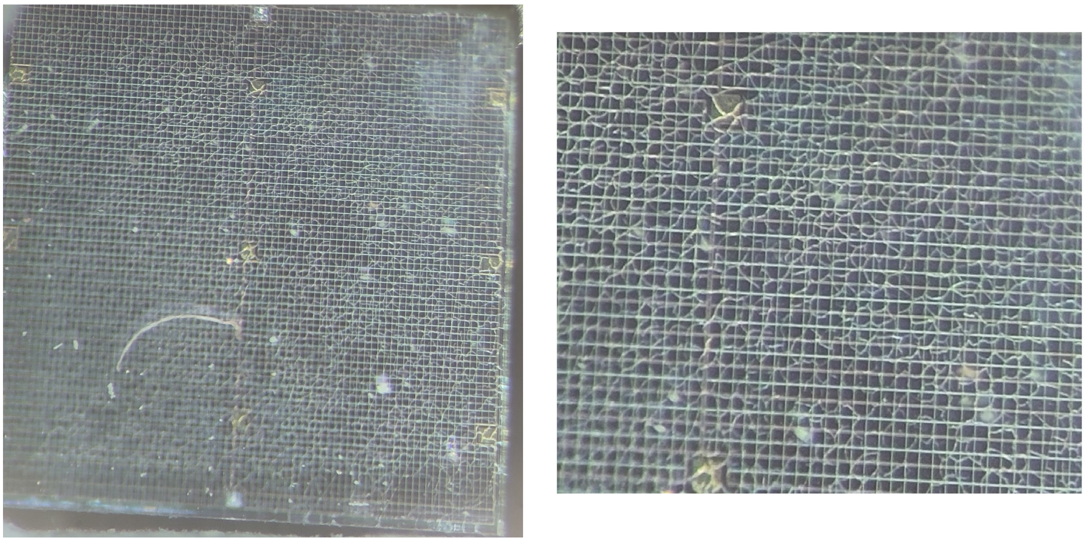

Figure 41: SiPM chip under a microscope after two thermal cycles with a zoomed in image on the right. Visible cracks were observed in the glass covering the chip.

4 Conclusions

The SiPM properties were characterized at room temperature and various cryogenic temperatures, down to 180 mK. The pulse shape of the SiPM changed from a pure slow exponential decay in room temperature into a combination of fast and slow components at cryogenic temperatures. The breakdown voltage was observed to decrease from 24.5 V down to a minimum value of 20.6 V at 40 K, and then increase again up to 21 V at 180 mK. The gain of the SiPM decrease monotonically and reduced by a factor of 4 at 5 K, compared to room temperature. Below 5 K the changes were minimal. The dark count rate of the SiPM decreased significantly already at liquid nitrogen temperature when the dark counts due to thermal excitation were suppressed. Below 40 K a secondary breakdown due to tunneling was observed, which set an upper limit for the bias voltage operating region. The photon detection efficiency of the SiPM could not be accurately measured, but an estimation of the PDE reducing by a factor of 25 was made. The relative PDE as a function of overvoltage was measured at 5 K and 180 mK.

Despite the reduced PDE and gain the SiPM could still be used as a single photon detector at 180 mK. Enormous reduction in the dark count noise (5 orders of magnitude) at low temperatures leads to an effective increase of the sensitivity by more than three orders of magnitude. The SiPM could withstand two thermal cycles with only some minor degradation visible, which did not effect any of its characteristics. The commercial availability and low price of the SiPM combined with the good performance makes it a good candidate for photodetection at cryogenic temperatures.

References

[1] H. Iams and B. Salzberg, Proceedings of the Institute of Radio Engineers **23**, 55 (1935).

[2] R. S. OHL, Light-sensitive electric device, 1941.

[3] K. G. McKay and K. B. McAfee, Physical Review **91**, 1079 (1953).

[4] K. G. McKay, Physical Review **94**, 877 (1954).

[5] J. Nishizawa, P-I-N Photo-Diode. Japanes Patent #JP1955-8969A, 1952.

[6] R. H. Haitz, Solid State Electronics **8**, 417 (1965).

[7] E. A. Gutierrez-D., M. J. Deen, and C. L. Claeys, *Low temperature electronics : physics, devices, circuits, and applications* (Academic Press , 2001), p. 964.

[8] M. Wiesinger *et al.*, Review of Scientific Instruments **94**, (2023).

[9] S. Sze and K. N. Kwok, *Semiconductor Devices: Physics and Technology* (John Wiley & Sons , 2006), p. 568.

[10] Storr, PN Junction theory for semiconductor diodes, 2022.

[11] S. Gundacker and A. Heering, The silicon photomultiplier: Fundamentals and applications of a modern solid-state photon detector, 2020.

[12] Onsemi, AND9770 - Introduction to the Silicon Photomultiplier (SiPM), 2023.

[13] Onsemi, J-Series SiPM Sensors Silicon Photomultipliers (SiPM), High PDE and Timing Resolution Sensors in a TSV Package J - Series SiPM Sensors, 2018.

[14] S. Jahromi and J. Kostamovaara, Optics Express **26**, 20622 (2018).

[15] T. Huang, Optical Engineering **44**, 074001 (2005).

[16] H. Otono, PoS **PD07**, 007 (2008).

[17] J. Zhang *et al.*, Journal of Instrumentation **17**, (2022).

[18] M. Biroth, P. Achenbach, W. Lauth, and A. Thomas, in *2016 IEEE Nuclear Science Symposium, Medical Imaging Conference and Room-Temperature Semiconductor Detector Workshop, NSS/MIC/RTSD 2016* (Institute of Electrical and Electronics Engineers Inc. , 2017), Vol. 2017-Janua.

[19] G. Collazuol *et al.*, in *Nuclear Instruments and Methods in Physics Research, Section A: Accelerators, Spectrometers, Detectors and Associated Equipment* (Elsevier , 2011), No. 1, pp. 389–392.

[20] R. H. Haitz, Journal of Applied Physics **36**, 3123 (1965).

[21] A. Cardini, V. Fanti, and A. Lai, IEEE Transactions on Nuclear Science **61**, 2672 (2014).

[22] T. Kiilerich and S. Ahopelto, [https://github.com/WaffleCoder4Life/GraduKoodia] (2024).

[23] H. Otono, H. Oide, S. Yamashita, and T. Yoshioka, Nuclear Instruments and Methods in Physics Research, Section A: Accelerators, Spectrometers, Detectors and Associated Equipment **610**, 397 (2009).

[24] S. Sze and K. K. Ng, *Physics of Semiconductor Devices* (Wiley , 2006).